Propeller Performance at Large Angle of Attack Applicable to Compound Helicopters

Stokkermans, T.C.A.; Veldhuis, L.L.M.

DOI
10.2514/1.J059509

Publication date
2021

Document Version
Accepted author manuscript

Published in
AIAA Journal: devoted to aerospace research and development

Citation (APA)
Stokkermans, T. C. A., & Veldhuis, L. L. M. (2021). Propeller Performance at Large Angle of Attack Applicable to Compound Helicopters. *AIAA Journal: devoted to aerospace research and development*, *59*(6), 2183-2199. https://doi.org/10.2514/1.J059509

Propeller Performance at Large Angle of Attack Applicable to Compound Helicopters

Tom C. A. Stokkermans* and Leo L. M. Veldhuis†
Delft University of Technology, 2629 HS Delft, The Netherlands

An experimental dataset is presented of propeller performance in static condition and at low subsonic airspeeds for various angles of attack up to 90 deg. Numerical investigation through a RANS CFD model revealed the mechanisms behind performance changes with advance ratio, angle of attack and configuration changes. The experimental dataset was found to be free of major errors and is very suitable for validation of propeller models. Furthermore, aerodynamic interaction with an upstream wing was tested with the propeller and wing normal to the flow, to represent the interaction occurring with a time-averaged main rotor slipstream on a compound helicopter. From numerical investigation it was concluded that the results are qualitatively representative of this interaction. The experimental data showed that addition of the wing results in a net reduction of all propeller performance quantities, with thrust reducing up to 20%. A thrust decreasing and increasing mechanism were found numerically. For most tested operating conditions, the wing resulted in a small decrease of propeller thrust-over-power ratio. Decreasing propeller advance ratio, increasing wing distance, and increasing flap deflection generally decreased the effect of the wing on thrust and power, however the influence of flap deflection was found to be small.

Nomenclature

B	=	Number of propeller blades
C_{F_y}	=	$F_y/\left(\rho_\infty n^2 D_\mathrm{p}^4\right)$ y-force coefficient
C_{F_z}	=	$F_z/\left(\rho_\infty n^2 D_\mathrm{p}^4\right)$ z-force coefficient
C_{M_y}	=	$M_y/\left(\rho_\infty n^2 D_\mathrm{p}^5\right)$ y-moment coefficient
C_{M_z}	=	$M_z/\left(\rho_\infty n^2 D_\mathrm{p}^5\right)$ z-moment coefficient
C_P	=	$P/\left(\rho_\infty n^3 D_\mathrm{p}^5\right)$ power coefficient
C_p	=	$(p - p_\infty)/q_\infty$ pressure coefficient
$C_{p,\mathrm{r}}$	=	$(p - p_\infty)/q_{\infty,\mathrm{r}}$ pressure coefficient in rotating reference frame

*Ph.D. Candidate, Flight Performance and Propulsion Section, Faculty of Aerospace Engineering, AIAA Member, tcastokkermans@gmail.com.
†Full Professor, Head of Flight Performance and Propulsion Section, Faculty of Aerospace Engineering, AIAA Member.

C_T = $T/\left(\rho_\infty n^2 D_\mathrm{p}^4\right)$ thrust coefficient

C_{T_r} = $8/\pi^3 C_T$ helicopter rotor thrust coefficient

c = Chord, m

$c_{F_y}(r)$ = $\left(\frac{1}{2}BF'_y\right)/\left(\rho_\infty n^2 D_\mathrm{p}^3\right)$ y-force coefficient distribution

$c_{F_z}(r)$ = $\left(\frac{1}{2}BF'_z\right)/\left(\rho_\infty n^2 D_\mathrm{p}^3\right)$ z-force coefficient distribution

$c_P(r)$ = $\left(\frac{1}{2}BP'\right)/\left(\rho_\infty n^3 D_\mathrm{p}^4\right)$ power coefficient distribution

$c_T(r)$ = $\left(\frac{1}{2}BT'\right)/\left(\rho_\infty n^2 D_\mathrm{p}^3\right)$ thrust coefficient distribution

D = Diameter, m

d = Distance, m

F = Force, N

F' = Force distribution, Nm^{-1}

h_i = Average cell size of grid i, m

J = $V_\infty/(nD_\mathrm{p})$ advance ratio

k = Turbulence kinetic energy, Jkg^{-1}

L = Length, m

M = Moment, Nm

M_tip = Helical tip Mach number based on n and V_∞

n = Propeller rotational speed, s^{-1}

P = Shaft power, W

P' = Power distribution, Wm^{-1}

p = Static pressure, Pa

q = Dynamic pressure, Pa

q_r = $0.5\rho\left((2\pi nr)^2 + V^2\right)$ dynamic pressure in rotating reference frame, Pa

R = Radius, m

Re = Reynolds number

r = Radial coordinate, m

S = Area, m^2

T = Thrust, N

T' = Thrust distribution, Nm^{-1}

T_C = $T/\left(\rho_\infty V_\infty^2 D_\mathrm{p}^2\right)$ thrust coefficient based on V_∞

t = Thickness, m

V = Velocity, ms^{-1}

V_d = Downwash farfield velocity, ms^{-1}

x = x-coordinate, m

y = y-coordinate, m

y^+ = Dimensionless wall distance

z = z-coordinate, m

α = angle of attack, deg

β = Blade pitch angle, deg

δ_f = Flap deflection, deg

δ_w = Boundary correction factor

μ = $V_\infty / V_\mathrm{tip}$ alternate advance ratio

ρ = Density, kgm^{-3}

φ = Propeller blade phase angle, deg

ω = Turbulence dissipation rate, $\mathrm{Jkg}^{-1}\mathrm{s}^{-1}$

Subscripts

0 = At static condition (V_∞ = 0 m/s)

$0.7R_\mathrm{p}$ = At blade section $r/R_\mathrm{p} = 0.7$

a = Axial

b = Blade

c = Corrected

mr = Main rotor

p = Propeller

t = Tangential

tip = Tip

ts = Test section

w = Wing

x = x-direction

y = y-direction

z = z-direction

∞ = Freestream

I. Introduction

Propeller propulsion is recently gaining renewed interest. Its inherently high propulsive efficiency due to a high mass flow rate and low velocity increase makes it suitable to reduce fuel consumption or enhance the performance of aircraft [1]. Furthermore, electrification of propulsion enables distribution of propellers to gain additional propulsive efficiency benefits from synergistic propulsion-airframe integration [2, 3]. One such application is electric vertical take-off and landing vehicles (eVTOL) [4–6] which use propellers from vertical take-off and landing to cruise for lift and/or thrust. To ensure performant vehicle-level designs, propellers on eVTOL vehicles must achieve good aerodynamic performance across a wide range of operating flight conditions.

A specific application where propellers enable a performance benefit through their inherently high propulsive efficiency and through propulsion integration is that of the Airbus RACER (Rapid And Cost-Effective Rotorcraft) compound helicopter [7–13] as depicted in Fig. 1 a. While helicopters are excellent for vertical take-off and landing, they only have a limited maximum speed: The asymmetric flow condition of the main rotor at high speed causes compressibility effects on the advancing blade side and stall on the retreating blade side of the main rotor that limit its lifting and propulsive capability [14, 15]. This compound helicopter overcomes the main rotor limitation at high speed by reducing rotational speed and using auxiliary lift from a box-wing and auxiliary thrust from wingtip-mounted propellers in pusher configuration. Such propellers experience a reduction in shaft power due to the swirling vortex inflow from the upstream wingtip in case the propeller rotates against the direction of the wingtip vortex [16–19]. Specifically for this helicopter, the interaction resulted in a propulsive efficiency increase up to 11% [8].

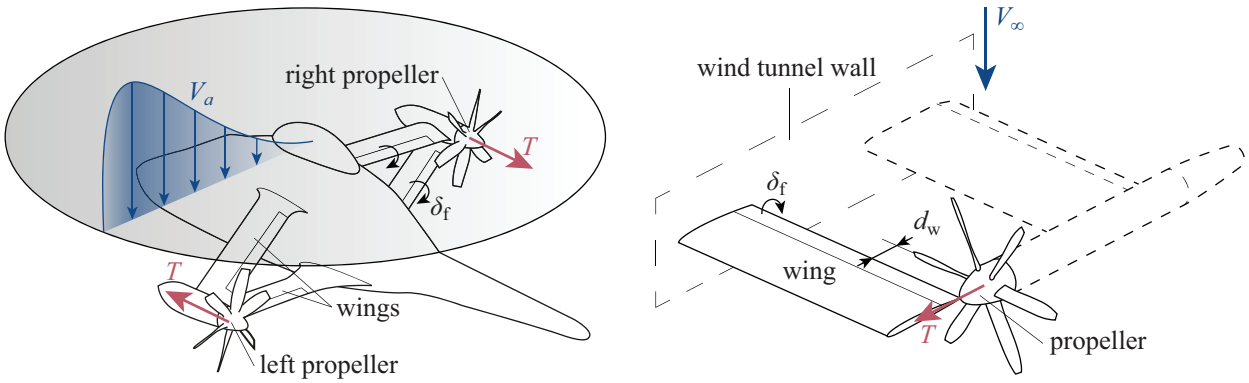

a) Airbus RACER in hover (without tailplanes). **b) Propeller and wing setup in wind tunnel.**

Fig. 1 Comparison of Airbus RACER compound helicopter to experimental setup of propeller and wing.

Similar to eVTOL vehicles, also for this compound helicopter the propellers experience a large range of angle of attack as in hover (and vertical flight) the main rotor slipstream causes a near perpendicular inflow, while in cruise the inflow angle induced by the main rotor is much smaller [11–13]. Interaction with the wings adds additional disturbances to the inflow of the propeller. In hover, as the propellers have to counter the torque of the main rotor, one propeller

(left) delivers forward thrust and the other (right) reverse thrust. In previous computational work in Ref. [11] it was shown that for the right propeller, where the wings are in the slipstream, the wings lead to a decrease of right propeller reverse thrust by 1.5% for equal blade pitch compared to the situation without wings. A much larger effect of the wings was found for the left propeller, where it alters the inflow and increases thrust by 10.5% with slightly reduced thrust-over-power ratio. On the contrary, in the computational study of Frey et al. [13] the wings lead to a decrease of left propeller thrust by 14.9%, while the right propeller reverse thrust decreased by 0.9%. This was however at different left and right propeller thrust from Ref. [11], and also other differences were present, e.g. a simulated instead of modeled main rotor and updated geometry. This different performance prediction highlights the sensitivity of the interaction effects to the specific conditions.

In this study the results of a wind tunnel experiment are discussed. The first part treats angle of attack effects on propeller performance up to a large angle of 90 deg. Some research has been performed on propellers at large angle of attack, e.g. Refs. [20–22] This experimental dataset complements the previous research with a modern scale propeller. To investigate the local loading and flowfield in more detail and to validate the model, the experimental data is complemented with RANS CFD simulations of the same setup. The presented data could serve as validation data for lower order propeller models used in the design process of for instance eVTOL vehicles. The data also serves as the baseline performance for the second part of the study.

In the second part the effects of aerodynamic interaction with a wing is investigated experimentally to replicate the situation occurring for the left propeller of the described compound helicopter in hover. This is again complemented with RANS CFD simulations. An approximation of the interaction on the compound helicopter was realized by installing a tractor propeller at 90 deg angle of attack in an 3/4 open jet wind tunnel and placing a separate planar wing with flap upstream of the propeller, such that the wingtip aligned with the propeller axis, see Fig. 1 b. In this setup the main rotor flow was approximated by the wind tunnel jet. The goal was to investigate the specific interaction problem in a simplified form by means of an experiment, in order to verify the numerical findings that were found for more complicated geometry. Furthermore, a second goal was to study parametrically the effects of propeller–wing spacing d_w and flap deflection δ_f on the propeller performance in the described situation. The results of this interaction problem may also be relevant for eVTOL concepts with wingtip-mounted pusher-propellers in the transition phase from vertical take-off to cruise.

This setup neglects any of the transient effects that the main rotor blade tip vortices and wakes have on the propeller loading as described by [10, 13]. Therefore, in terms of main rotor flow this wind tunnel dataset is of similar fidelity as the computational results in Refs. [8, 11], where the main rotor flow was approximated with a non-uniform actuator-disk. Furthermore, the experiment approximates the main rotor slipstream flowfield as uniform in space, while in reality a strong radial variation in axial induced velocity exists (as sketched in Fig. 1 a) and a much smaller tangential velocity component is present too. The effect of this non-uniformity is investigated numerically in this study, but the tangential

component is not considered.

II. Experimental Setup

A. Wind-Tunnel Facility and Models

The experiments were performed in Delft University of Technology's Open Jet Facility (OJF). This open-jet closed-circuit wind-tunnel features a maximum freestream velocity of about 30 m/s from the octagonal outlet of 2.85×2.85 m. The settling chamber is equipped with a honeycomb flow rectifier and five screens to remove spatial velocity deviations and to reduce the turbulence level of the flow. This results in velocity deviations below 0.5% in the vertical plane at 2 m downstream of the outlet, and a longitudinal turbulence intensity level below 0.24%. The contraction and outlet of the tunnel can be seen in Fig. 2 a.

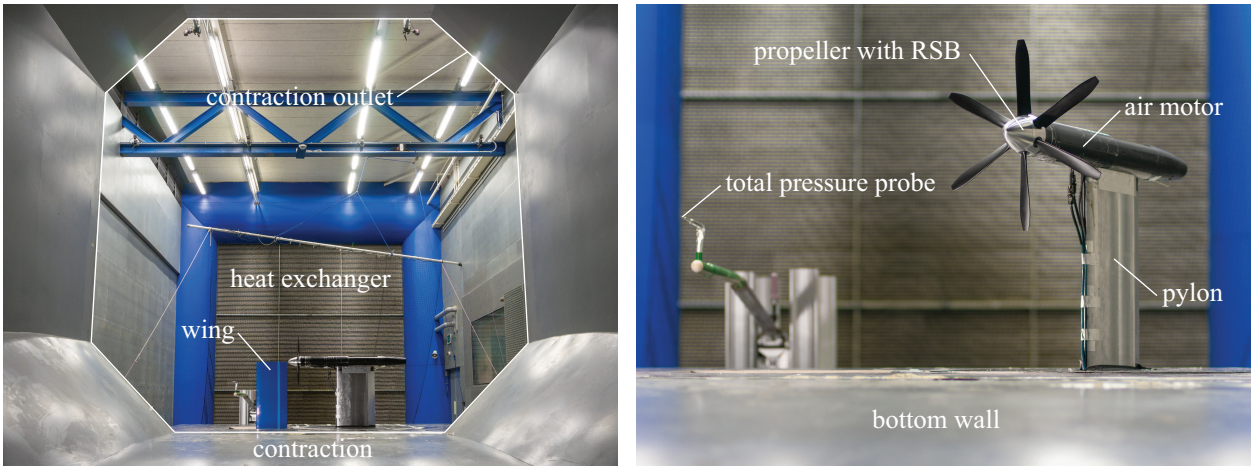

a) Propeller with wing in Open Jet Facility. **b) XPROP propeller at α_p = 45 deg.**

Fig. 2 Photos of experimental setup in the Open Jet Facility (OJF) at Delft University of Technology.

The 6-bladed XPROP propeller from Delft University of Technology was selected for this experiment, used by e.g. Refs. [23, 24]. It is a propeller with blade radius of $R_p = 0.2032$ m, and it was used at a blade pitch of $\beta_{0.7R_p} = 20$ deg and 30 deg. The propeller is shown in Fig. 2 b and the blade design is depicted in Fig. 3 in terms of radial distributions of chord, thickness, blade pitch and airfoils and is typical for turboprop airplanes. It does not feature sweep. In *Supplemental Data S1* a complete description of the blade design including airfoil sections is given.

The propeller was driven by a TDI 1999 turbine air motor, mounted in a nacelle on top of a pylon, see Fig. 2 b. The dimensions of this setup are shown in Fig. 4. The pylon was fixed to a turn table to allow change of propeller angle of attack α_p from 0 deg to 90 deg. No angle larger than 90 deg was considered, since at larger angles the exhaust of the air motor at the rear of the nacelle would have been disturbed by the wind tunnel jet. The bottom wall of the wind tunnel contraction outlet was extended beyond the pylon, effectively creating a 3/4 open jet test section.

To study interaction effects, a straight, cambered wing of chord $c_w = 0.240$ m with $0.25c_w$ flap was positioned in

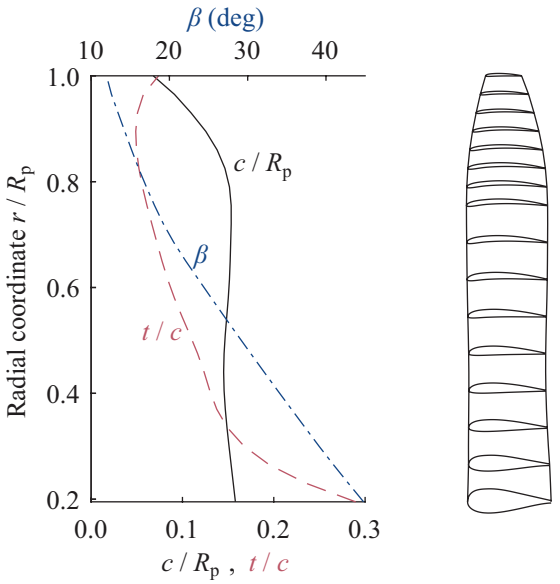

Fig. 3 XPROP propeller blade description for $\beta_{0.7R_p}$ = 20 deg with untwisted blade geometry and airfoils.

front of the propeller for α_p = 90 deg, see Fig. 2 a, with the wing planform perpendicular to the freestream flow. Its dimensions are also provided in Fig. 4. The chordwise distance of the wing to the propeller d_w and the flap deflection δ_f could be varied, as this was of interest to see if the effect of the wing on the propeller performance could be reduced. CAD models of the various propeller setups, as used for the CFD simulations, are attached to the paper as *Supplemental Data S2*.

B. Measurement Techniques

The measurements consisted mainly of force and moment measurements of the propeller with spinner. This was achieved with a custom 6-component rotating shaft balance [25]. This sensor has a range of ±344.1 N for the thrust, ±200 N for the in-plane forces, ±28.7 Nm for the torque and ±20 Nm for the out-of-plane moments. The root mean square (rms) full scale error in a rotating reference frame, obtained from applying a series of static load cases with known weights, are 0.02% for the thrust, 0.23% and 0.14% for the in-plane forces, 0.05% for the torque, and 0.13% and 0.10% for the out-of-plane moments, respectively. The sensor was attached to two 24 bit data acquisition cards with custom Labview data acquisition software and data were gathered at each measurement point with 10,000 Hz sampling frequency in a sweep of rotational speeds. An up- and down-sweep in rotational speed and a separate up-sweep was performed for each measurement condition with a measurement time of 10 s and 15 s respectively for cases without wing and 15 s and 20 s respectively for cases with wing. Different measurement times were chosen for the same measurement condition to establish confidence that the measurement time was sufficient to average out unsteady effects. The cases with wing were measured for a longer time because of the increased unsteadiness of the propeller loading due to the wing.

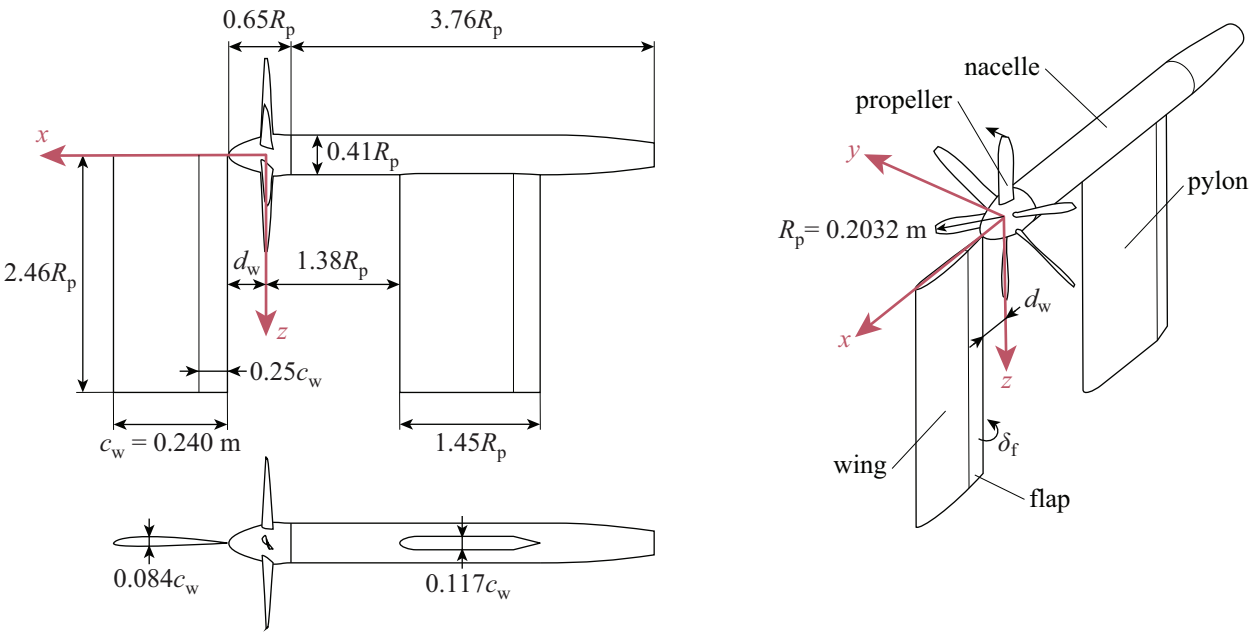

Fig. 4 Side, bottom and isometric view of propeller setup at α_p = 90 deg with wing, including dimensions.

A zero measurement was taken before and after each sweep to minimize the effect of drifts on the results. The zero measurements were applied to the data using a linear fit based on the zeros and the measurements timestamps. With an air supply control system, the rotational speed of the air motor was set. All measurements were taken at frequencies above the eigenfrequency of the propeller test stand and multiples of the eigenfrequency were also avoided. The rotating components, so the propeller blades, hub, spinner and the RSB have been spin balanced on a Schenck type M466 balancing machine according to ISO standard 1940. Maximum peak-to-peak fluctuations in rotational speed of typically 0.5% were found during the measurements for the cases without wing and 1.1% for the cases with wing. Based on the recorded one-per-revolution trigger signal, the force and moment data were phase-averaged, a reference frame transformation was applied from a rotating reference frame to a stationary frame, and the data were corrected for the mass of the propeller with spinner. Based on the three repeated measurements of the same condition, 95% simultaneous confidence bands were calculated. Confidence intervals based on these bands are plotted in the results throughout the paper.

Besides the balance measurements, a Kiel probe was used to measure total pressure for reference as shown in Fig. 2 b. Furthermore, the wing was instrumented with tufts to visualize the shearlines on its surface under the influence of the propeller. The loading on the wing was not measured as this study focused on propeller performance effects.

C. Wind Tunnel Wall Corrections

Several wind tunnel wall corrections should be considered when testing in an open jet tunnel with a propeller model. First, an inflow velocity correction due to blockage was considered based on Sayers and Ball [26]: This resulted in a

corrected advance ratio of $J_c \approx 1.03J$ with a blockage area of 4.3% of the contraction outlet cross-sectional area, based on the worst case scenario of the propeller setup and wing at 90 deg angle of attack. Furthermore, a correction of the advance ratio is needed due to the sink effect of the propeller when operating at small angle of attack. The method discussed by Hackett et al. [27] for a closed-section wind tunnel was extended for application to an open jet tunnel by Prof. G. Eitelberg (personal communication, November 9, 2018). The corrected advance ratio in this method is equal to:

$$J_c = \frac{J}{1 + \frac{S_p}{S_{ts}} \left(\sqrt{1 + \frac{8}{\pi} T_C \cos\left(\alpha_p\right)} - 1 \right)} \tag{1}$$

where S_p is the area of the propeller disk, S_{ts} the contraction outlet cross-sectional area and T_C the thrust coefficient based on freestream. The thrust coefficient is multiplied by $\cos\left(\alpha_p\right)$ to get only the component of the thrust in wind tunnel axial direction in case of a nonzero angle of attack. This correction was applied to the wind tunnel data with freestream flow without wing, and results are shown in Fig. 13.

The last considered wall correction corrects the angle of attack when operating the propeller at large angles of attack following the method of Langer et al. [28]. The method assumes that the propeller thrust is equivalent to lift in the classical Glauert wall correction method. The required angle of attack correction then is:

$$\Delta\alpha_p = \frac{2\delta_w C_{T_r} \sin\left(\alpha_p\right) S_p}{\mu^2 S_{ts}} \tag{2}$$

where δ_w is the boundary correction factor, C_{T_r} the thrust coefficient as defined for helicopter rotors, and μ the alternate advance ratio defined as V_∞ / V_{tip}. The thrust coefficient is multiplied by $\sin\left(\alpha_p\right)$ to get only the component of the thrust normal to the freestream velocity, i.e. the lift. A value of $\delta_w = -0.14$ was assumed, slightly reduced compared to open jet tunnel value in Langer et al. [28], since this setup is effectively a 3/4 open jet, and based on observation of the values in Barlow et al. [29]. Note that this assumption is quite uncertain. The angle of attack correction was applied to the wind tunnel data with freestream flow without wing, and results are shown in Fig. 13.

A correction for buoyancy was not considered in this research, since the body of interest has a relatively small dimension in the wind tunnel axial direction.

D. Analyzed Test Cases

An overview of the analyzed test cases is given in Table 1. The isolated propeller performance without wing named PNP (Propeller-Nacelle-Pylon) was measured at $V_\infty = 0$ m/s, and with freestream airspeed for $0 \leq \alpha_p \leq 90$ deg. Propeller angle of attack α_p is defined with respect to the propeller axis like in Serrano et al. [30], and was achieved by rotating the propeller setup around the z-axis. Up- and downsweeps of propeller rotational speed (3400 – 7600 rpm) were performed to vary helical tip Mach number M_{tip} in static condition (zero freestream airspeed) and advance ratio J

when there was a freestream airspeed. This was done for a propeller blade pitch of $\beta_{0.7R_p} = 20$ deg and $\beta_{0.7R_p} = 30$ deg. Based on these results, results with wing, named PNWP (Propeller-Nacelle-Wing-Pylon), were only measured for $\beta_{0.7R_p} = 20$ deg to prevent significant flow separation on the blades at large α_p. Furthermore, no measurements with wing at $V_\infty = 6$ m/s were performed because of the considerable angle of attack wall correction required for this airspeed. The experimental data for the PNP and PNWP configuration are attached to the paper as *Supplemental Data S3*, including 3rd order polynomial fits of the propeller performance data as function of M_{tip} in static condition and J when there was a freestream airspeed.

Table 1 Overview of analyzed experimental test cases.

config.	$\beta_{0.7R_p}$ (deg)	V_∞ (m/s)	α_p (deg)	d_w/R_p	δ_f (deg)
PNP	20, 30	0	0	-	-
PNP	20, 30	6, 12, 18	0, 15, 30, 45, 60, 75, 90	-	-
PNWP	20	12, 18	90	0.4, 0.65, 0.9, 1.4	0
PNWP	20	12, 18	90	0.4	0, 10, 20

III. Computational Setup

A. Geometry

Five different geometries were simulated with RANS CFD simulations:

SBP Single blade passage of the propeller and nacelle at $\alpha_p = 0$ deg.

PN Full annulus propeller and nacelle without pylon at various α_p.

PNP Full annulus propeller and nacelle with pylon at various α_p.

PNW Full annulus propeller and nacelle with wing without pylon at $\alpha_p = 90$ deg, $d_w/R_p = 0.4$ and $\delta_f = 0$ deg.

PNWP Full annulus propeller and nacelle with wing and pylon at $\alpha_p = 90$ deg, $d_w/R_p = 0.4$ and $\delta_f = 0$ deg.

The geometry was the same as in the experiment as shown in Figs. 3 and 4. A simplification was present near the blade root, which has a cutout at the trailing edge in the experiment and continues to the spinner wall in the simulations. The wing flap was not modeled as only zero degree flap deflection cases were simulated.

B. CFD Solver Setup

Simulations were performed with ANSYS Fluent 18.1 [31], a commercial, unstructured, cell-centered, finite volume solver. The ideal-gas law was applied as equation of state, whereas the dynamic viscosity was obtained with Sutherland's law. Standard sea level atmospheric conditions were assumed [32]. Discretization of the advection term was done with an upwind scheme using the Barth–Jesperson boundedness principle [33] and time-dependent solutions were found by a 2nd order backward Euler scheme. Steady solutions were obtained using the pseudo transient under-relaxation method. Initial conditions were calculated using the full multigrid initialization method. A timestep equivalent to

1 deg of propeller rotation was used for the transient results as commonly found in propeller research [34, 35]. For the PNWP configuration, the most complex case, a simulation was performed with a timestep equivalent to 0.5 deg and 2 deg of propeller rotation, to check the temporal resolution. The Spalart–Allmaras (SA) one-equation turbulence model [36] was selected with modification proposed by Dacles-Mariani et al. [37] to prevent build-up of turbulence viscosity in vortex cores. Values for the inlet turbulence were based on the recommendations by Spalart and Rumsey [38] meant for general use for most typical external aerodynamic applications, which resulted in an eddy viscosity ratio of 0.21044. For the PNWP configuration a simulation was performed with the two-equation eddy viscosity $k-\omega$ model with shear stress transport correction ($k-\omega$ SST) [39] to check the effect of turbulence modeling on the results. Also for this model, values for the inlet turbulence were based on Ref. [38] with $k = 1 \cdot 10^{-6} V_\infty^2$ and $\omega = 5V_\infty/L$ where L is a reference length, in this case the mean blade chord.

C. Domain and Boundary Conditions

Two different computational domains were used, a domain for a single blade passage (SBP) of the isolated propeller and nacelle at $\alpha_p = 0$ deg and a domain for all full annulus propeller simulations. The single blade passage domain including boundary conditions and dimensions is shown in Fig. 5. Since the wake of a propeller with axisymmetric nacelle is cyclic with the number of the blades, only a single blade could be modeled with periodic boundary conditions in a 60 deg wedge domain to reduce the computational cost, similar to e.g. Ref [40]. The outer dimensions of the domain were chosen to be sufficiently large with respect to the propeller radius, in order to minimize the influence of the boundary conditions on the flow properties near the propeller.

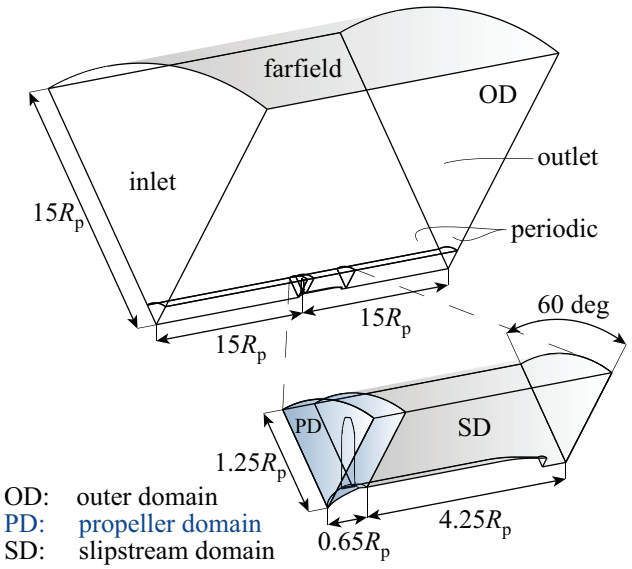

Fig. 5 Computational domain for a single blade passage of the isolated propeller at zero angle of attack.

For simulations with freestream flow, at the domain inlet a total-pressure jump with respect to the undisturbed static

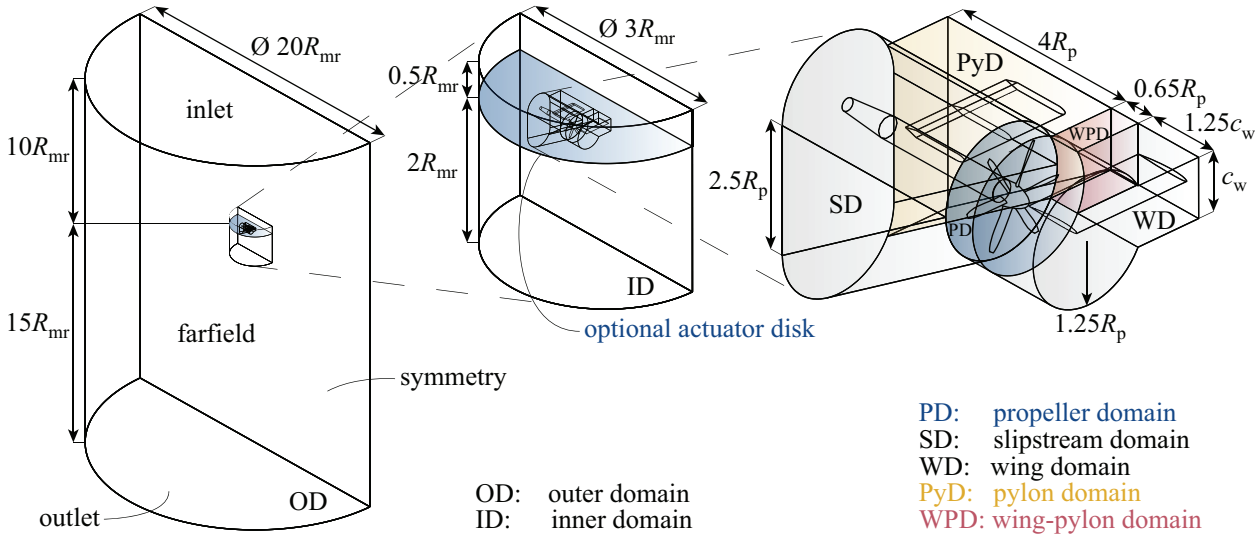

Fig. 6 Computational domain for the full annulus propeller simulations at angle of attack and propeller–wing simulations with freestream or actuator-disk approach.

pressure was set to reach the desired freestream airspeed. Furthermore, the freestream total temperature was specified. At the domain outlet, the static pressure was prescribed to be on average equal to the freestream static pressure. A Riemann-invariant pressure farfield condition was specified with a Mach number, static pressure and static temperature complying with the inlet conditions.

For simulations at static condition, on the inlet, farfield and outlet the static pressure was prescribed to be on average equal to undisturbed static pressure. Especially this condition required the large $15R_p$ distance of the boundaries from the propeller. By applying a reference frame transformation to the subdomain around the propeller (PD) and slipstream (SD) with the multiple reference frame model (MRF), propeller motion was simulated. A sliding mesh interface was present around the propeller domain. The propeller and spinner walls were modeled with a no-slip condition and the nacelle was modeled with a moving wall, stationary in the absolute frame to counter the local reference frame transformation.

The propeller domain was copied and rotated to arrive at a full annulus propeller. The domain for the full annulus propeller simulations is shown in Fig. 6. This half cylindrical domain featured a symmetry boundary condition on the rectangular face, to approximate the single wind tunnel wall in the 3/4 open jet configuration. For the simulations without wing and for some of the simulations with wing where a freestream airspeed was present, the same inlet, outlet and farfield conditions were set as for the single blade passage simulations. For the other simulations with wing, a non-uniform actuator-disk (AD) was used to replace the freestream flow, to simulate the axial and radial flow of a helicopter main rotor in hover, similar to Ref. [41]. For these simulations the static pressure on the inlet, farfield and outlet was prescribed to be on average equal to freestream static pressure. The actuator-disk approach from previous research in Ref. [40] was used with a thrust loading distribution based on the experimental data of the UH60 blade

presented in Srinivasan et al. [42]. The UH60 data provides a realistic main rotor loading distribution in hover to introduce a typical radial non-uniform downwash distribution. Only the radial shape of the loading was used as the thrust level was tuned such that the downwash farfield velocity V_d was equal to the freestream airspeed V_∞ in the wind tunnel following simple momentum theory [43]:

$$T_\mathrm{mr} = \frac{1}{2}\rho_\infty V_\mathrm{d}^2 S_\mathrm{mr} = \frac{1}{2}\rho_\infty V_\infty^2 \pi R_\mathrm{mr}^2 \tag{3}$$

The main rotor diameter was chosen equal to the width of the contraction outlet, resulting in $R_\mathrm{mr} = 1.425$ m. The actuator-disk center coincided with the wing quarter-chord line and the distance between the main rotor and propeller was similar to the compound helicopter in Ref. [8]. The outer dimensions of the domain were chosen sufficiently large with respect to the main rotor radius ($\geq 10R_\mathrm{mr}$), larger than the $5R_\mathrm{mr}$ distance in Potsdam and Strawn [44] and larger than the largest tested distance of $9R_\mathrm{mr}$ in Strawn and Djomehri [45].

The wing, pylon and wing-pylon domain were only present when these parts were simulated. For the simulations without wing, the propeller, slipstream and pylon domain could be turned to achieve the desired propeller angle of attack. The slipstream domain was shaped such that it captured the propeller slipstream for all tested angles of attack and operating conditions. Grid rotation of the propeller domain with sliding mesh interfaces was used to simulate propeller motion. All geometry walls were modeled with a no-slip condition.

D. Grid and Grid Dependency Study

Unstructured grids were constructed by means of ANSYS Meshing. For regions adjacent to geometry walls, the unstructured grid was made up of a triangular wall mesh, followed by layers of semi-structured prismatic elements of the inflation layer. For the remainder of the domain tetrahedral elements were used. Grid density in the whole domain was controlled by wall refinement of all no-slip walls, volume refinement of the various subdomains, a 1$^\mathrm{st}$ layer thickness of the inflation layers, and growth rates of the inflation layers and the remainder of the grid. The 1$^\mathrm{st}$ layer thickness was tuned to comply with the y^+ requirement of the turbulence models of $y^+ \leq 1$. Especially for the propeller and slipstream domains a dense grid was used to model the propeller slipstream flow-structure accurately. For the full annulus propeller simulations, the grid of the propeller domain from the single blade passage setup was copied and rotated to achieve periodicity in the grids.

Grid dependency results are presented alongside the results. All refinements were varied systematically in the grid dependency study, except for the inflation layer which was kept constant in line with Roache [46]. To estimate discretization uncertainty, the least-squares version of the grid convergence index (GCI) proposed by Eça and Hoekstra [47] was applied. The procedure as discussed in Ref. [40] was used. In Table 2 the grid sizes are given for the simulation configurations for which a grid study was performed. For the single blade passage (SBP) configuration and the full

Table 2 Grid sizes for the grid dependency study of the SBP, PNP and PNWP configurations.

	SBP		PNP		PNWP	
grid	# of cells	h_i/h_1	# of cells	h_i/h_1	# of cells	h_i/h_1
4	757,740	2.06	3,931,491	2.24	4,287,815	2.29
3	1,382,195	1.68	7,616,247	1.80	8,663,777	1.81
2	2,829,218	1.33	17,418,655	1.37	21,578,647	1.33
1	6,605,436	1.00	44,453,771	1.00	51,243,373	1.00

annulus configurations with pylon (PNP and PNWP), four grids were constructed, of which the densest grid was used for the final results. For the configurations without pylon, only the densest grid was made, since grid study results of the other, more complex configurations were considered to be representative.

IV. Results without Wing Interaction

First, propeller performance results are discussed without wing interaction, to serve as reference for the cases with wing and to characterize performance at large angle of attack. The propeller reference frame, blade phase angle φ, angle of attack α_p, freestream velocity components and force components are defined in Fig. 7. In the next two sections, first the propeller performance at zero angle of attack is treated in Section IV.A and then at non-zero angle of attack in Section IV.B.

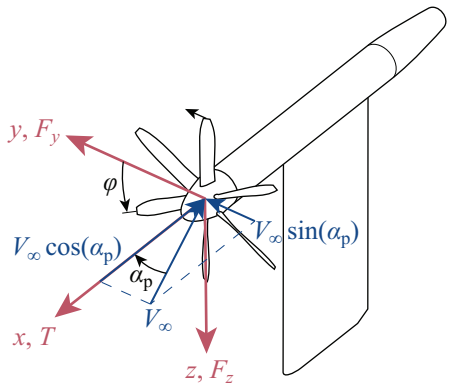

Fig. 7 Sketch of propeller setup without wing, including definition of propeller reference frame, blade phase angle φ, angle of attack α_p, freestream velocity components and force components.

A. Propeller Performance at Zero Angle of Attack

The baseline propeller integral performance at zero angle of attack is plotted in Figs. 8 and 9 in static condition and at freestream airspeeds of V_∞ = 6 m/s, 12 m/s and 18 m/s respectively. Thrust coefficient C_T and power coefficient C_P are plotted versus tip Mach number M_tip in static condition and versus advance ratio J with freestream airspeed for the two blade pitch angles $\beta_{0.7R_\mathrm{p}}$ = 20 deg and 30 deg. The raw experimental data are plotted together with 3$^\mathrm{rd}$ order

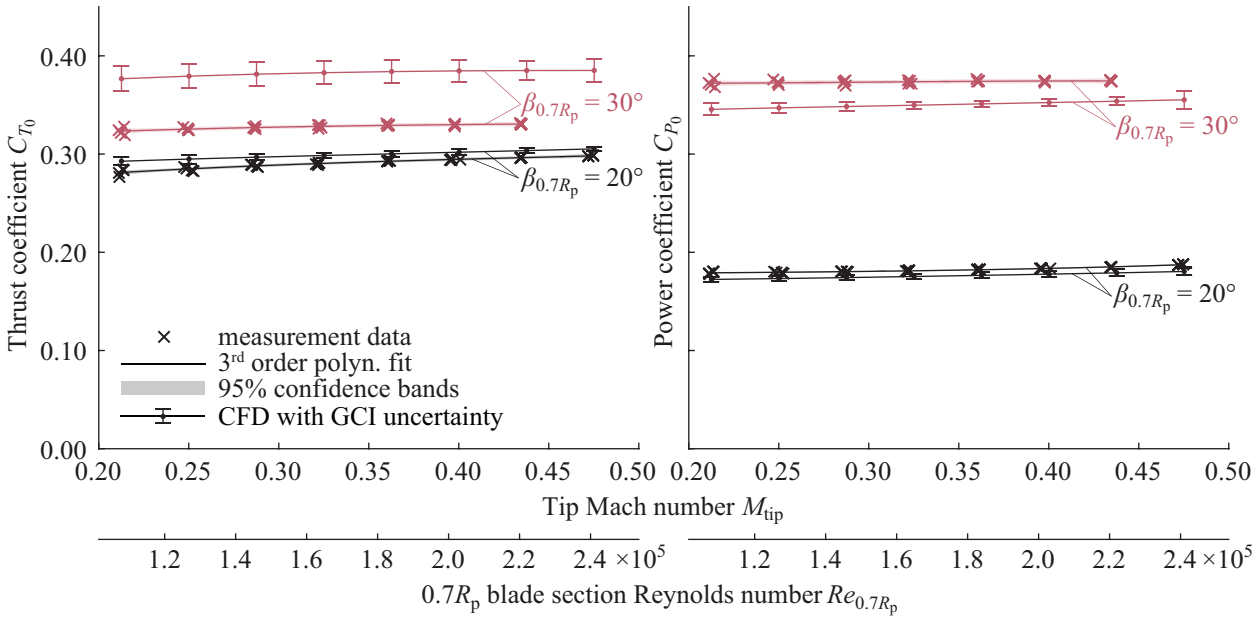

Fig. 8 Thrust and power coefficient comparison between experiment and CFD for V_∞ = 0 m/s.

polynomial fits with 95% simultaneous confidence bands. Furthermore, RANS CFD predictions with GCI uncertainty are shown from steady simulations with the MRF approach, using the domain depicted in Fig. 5.

The performance measured experimentally in static condition is characterized by a very minor dependency on tip speed. This is partly due to the relatively small range that could be achieved in the experiment. These results are in line with McLemore and Cannon [20], where a much larger range of tip Mach number was tested and also only a minor dependency of C_T and C_P on M_{tip} was found for most blade pitch angles. A small increase in thrust and power coefficient is visible for both blade pitch angles with increasing tip Mach number or section Reynolds number. While C_{T_0} increases by approximately 10% when increasing blade pitch angle from $\beta_{0.7R_p}$ = 20 deg to 30 deg, C_{P_0} increases much more, by approximately 100%. This indicates flow separation for the larger blade pitch angles, as will be shown later. The CFD prediction for $\beta_{0.7R_p}$ = 20 deg is very accurate both in terms of power and thrust for the whole tip speed range, while for $\beta_{0.7R_p}$ = 30 deg the thrust is largely over-predicted and the power under-predicted. The earlier mentioned expected flow separation is the likely cause of this difference in prediction. The GCI uncertainty is also considerably higher for the larger blade pitch angle, especially in terms of thrust.

At the lowest advance ratio for V_∞ = 6 m/s, the experimental thrust and power coefficients in Fig. 9 are very similar to those in static condition. With increasing advance ratio through decreasing rotational speed, both C_T and C_P decrease. The data for the three freestream airspeeds (V_∞ = 6, 12 and 18 m/s) in Fig. 9 follow the same trends with advance ratio, but small differences for the overlapping advance ratios are noticeable. These differences are a result of Reynolds number differences. The increase in thrust coefficient with increase in blade pitch angle is larger for higher advance ratios, while for the power coefficient the increase remains more or less constant. This indicates that flow separation is

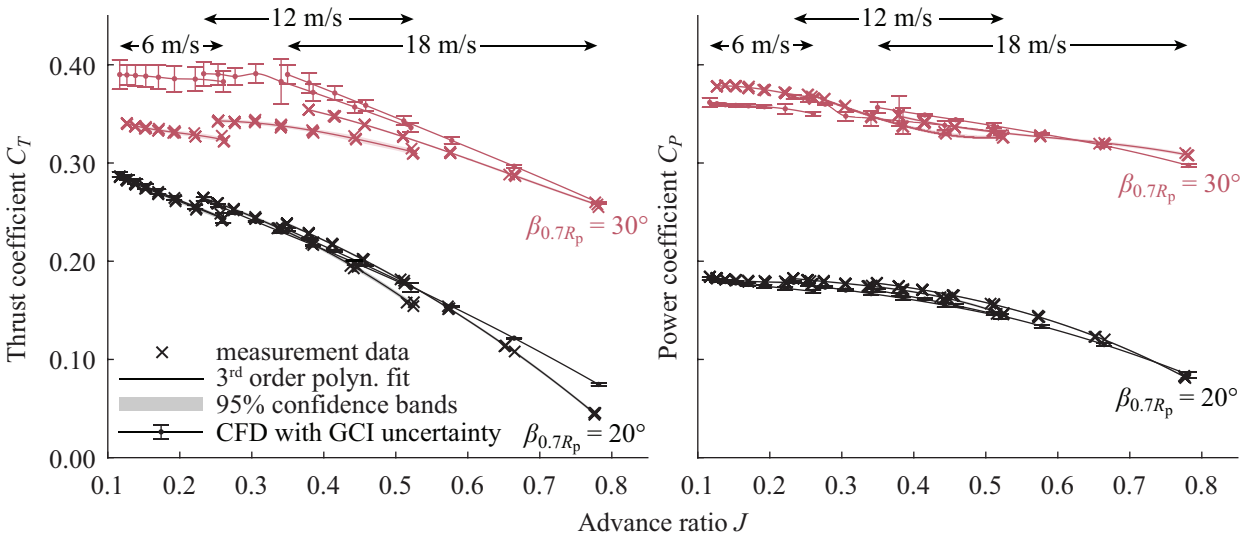

Fig. 9 Thrust and power coefficient comparison between experiment and CFD at freestream airspeeds for $\alpha_p = 0$ deg.

likely less severe for these higher advance ratios. The maximum error in the CFD prediction for thrust occurs at the lower advance ratios for $\beta_{0.7R_p} = 30$ deg. The GCI uncertainty in the CFD prediction is also higher in that area. For $\beta_{0.7R_p} = 20$ deg the maximum error in the CFD prediction for thrust occurs at the higher advance ratios. The CFD prediction for power is generally better than the thrust prediction.

To investigate what is happening on the propeller blades in the CFD simulations, in Fig. 10 the thrust and power distribution along the radius are plotted for two specific conditions for both blade pitch angles. Furthermore, in Fig. 11 the shearlines (lines following the shear stress vector direction) and pressure distribution on the blade are shown for the same conditions. Results at the same rotational speed for $V_\infty = 0$ m/s and 18 m/s are plotted alongside each other. For $\beta_{0.7R_p} = 20$ deg in static condition, the thrust distribution is characterized by a maximum relatively outboard at $r/R_p = 0.93$ compared to at $r/R_p = 0.85$ with the non-zero airspeed. For both conditions at $\beta_{0.7R_p} = 20$ deg, a narrow peak is visible near the tip of blade, resulting from the low static pressure in the vicinity of the tip vortex. This is also visible in the static pressure contour by the region of negative $C_{p,r}$ along almost the entire chord near the tip. For the power coefficient, a maximum in both conditions is found around $r/R_p = 0.8$ with again narrower peaks near the tip. For these conditions, no significant flow separation is indicated by the shearlines, only a small region of flow separation near the trailing edge for $r/R_p < 0.6$ in static condition.

For $\beta_{0.7R_p} = 30$ deg in static condition, the peak in thrust moves inboard to $r/R_p = 0.9$ and the peak at the blade tip disappears, as flow separation over the entire chord occurs in the tip region and furthermore near the trailing edge for lower radial locations. As a result, the power coefficient increases drastically, and its maximum occurs at $r/R_p = 0.9$ in the region with significant flow separation. At $V_\infty = 18$ m/s, the thrust and power distribution for $\beta_{0.7R_p} = 30$ deg are very similar in terms of shape to that of $\beta_{0.7R_p} = 20$ deg. For the larger blade pitch angle, a region of trailing edge

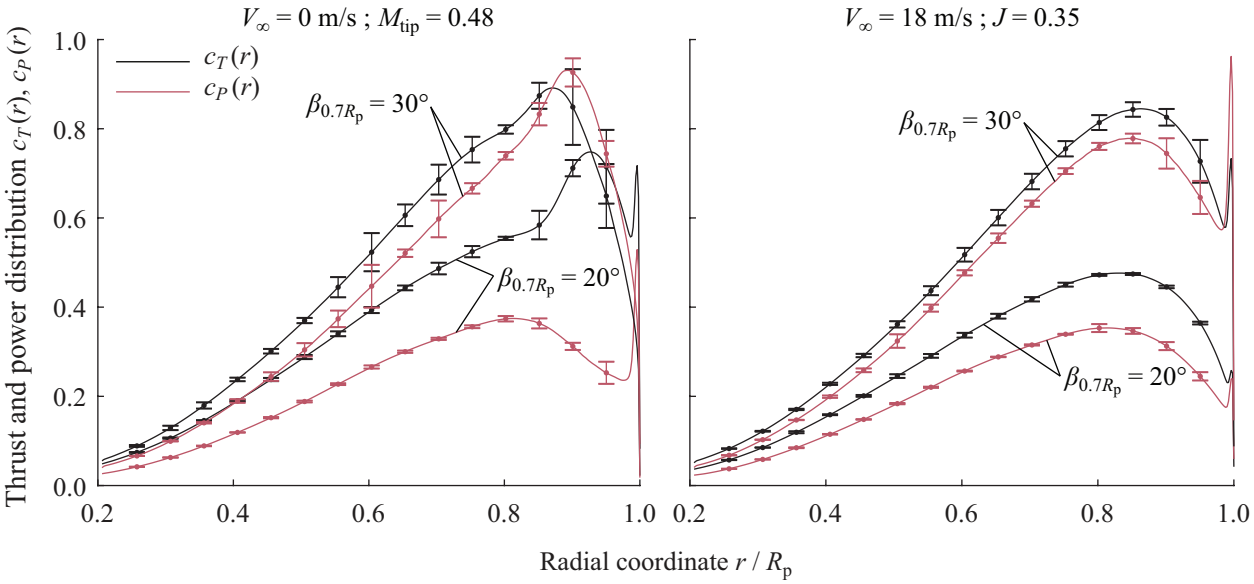

Fig. 10 CFD result showing thrust and power coefficient distribution for four selected conditions at α_p = 0 deg.

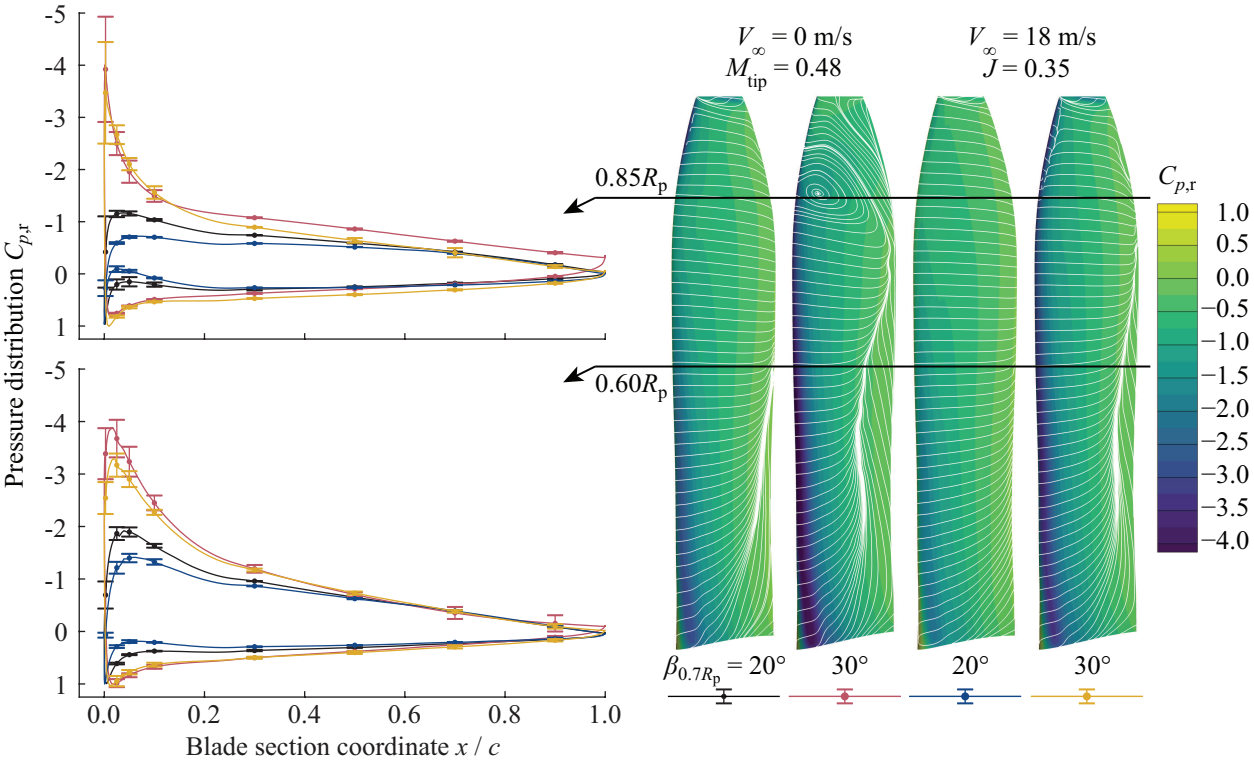

Fig. 11 CFD results showing blade shearlines and pressure coefficient distribution with discretization uncertainty for four selected conditions at α_p = 0 deg.

separation is indicated by the shearlines, which does not seem to change the loading characteristics significantly.

In conclusion, for $\beta_{0.7R_p} = 20$ deg, CFD predictions of the propeller performance are accurate and only minor flow separation occurs. For $\beta_{0.7R_p} = 30$ deg, especially in static condition or for very low advance ratios, the CFD predictions contain significant error with respect to the experiment, likely due to differences in predicting the occurring flow separation. Since propeller performance at large angle of attack is characterized by similar blade loading as in static condition during parts of the azimuth as the component of the velocity normal to the propeller becomes small, at angle of attack only results for $\beta_{0.7R_p} = 20$ deg are shown in the remainder of the study.

B. Propeller Performance at Non-Zero Angle of Attack

An angle of attack range from 0 deg to 90 deg was investigated experimentally for the isolated propeller. The performance data and 3rd order polynomial fits with 95% simultaneous confidence bands are presented in Fig. 12 as function of advance ratio for all angles of attack and freestream airspeeds. The performance quantities are shown in the (tilted) hub frame of reference as depicted in Fig. 7. The results for the different freestream airspeeds do not match exactly as expected, because of differences in Reynolds number. With decreasing advance ratio, the thrust and power coefficient curves for different α_p all converge to the values found in static condition (Fig. 8). While for the smaller angles of attack C_T and C_P decrease with J, for $\alpha_p > 60$ deg they increase. In terms of in-plane forces, C_{F_y} is the dominant component compared to C_{F_z} as the angle of attack is formed by rotation around the propeller z-axis. For all advance ratios, with increasing angle of attack C_{F_y} increases up to a certain maximum angle, which for the highest J is found at an angle smaller than 90 deg. The effect of angle of attack on the performance quantities is larger for higher J, as the contribution of the freestream airspeed to the effective velocity becomes relatively larger due to the lower propeller rotational speed. The out-of-plane moments follow similar trends as the in-plane forces, with C_{M_y} the more dominant component compared to C_{M_z}. The mechanisms behind the angle of attack effects are discussed later in this section by means of the CFD results.

Since the experimental data were obtained in an open jet wind tunnel, wall corrections need to be considered. In Fig. 13, an estimation of the angle of attack and advance ratio correction are presented for the data in Fig. 12 based on Eqs. (2) and (1). This figure gives an indication of the required correction and all other results in this section are uncorrected. The advance ratio correction is presented as the difference between the corrected and measured advance ratio $\Delta J = J_c - J$. The data at the freestream airspeed of 6 m/s require a large angle of attack correction while at the highest advance ratio for 18 m/s the correction is almost negligible. The effect of these large corrections for 6 m/s on the corrected performance data is however small as in Fig. 12 it was shown that the dependency of the performance results on angle of attack for 6 m/s is relatively small. Furthermore, the advance ratio correction is relatively small for all operating conditions, although most pronounced again for the lowest airspeed of 6 m/s. Based on these correction estimates, for the interaction study with the wing in Section V only results at 12 m/s and 18 m/s are presented.

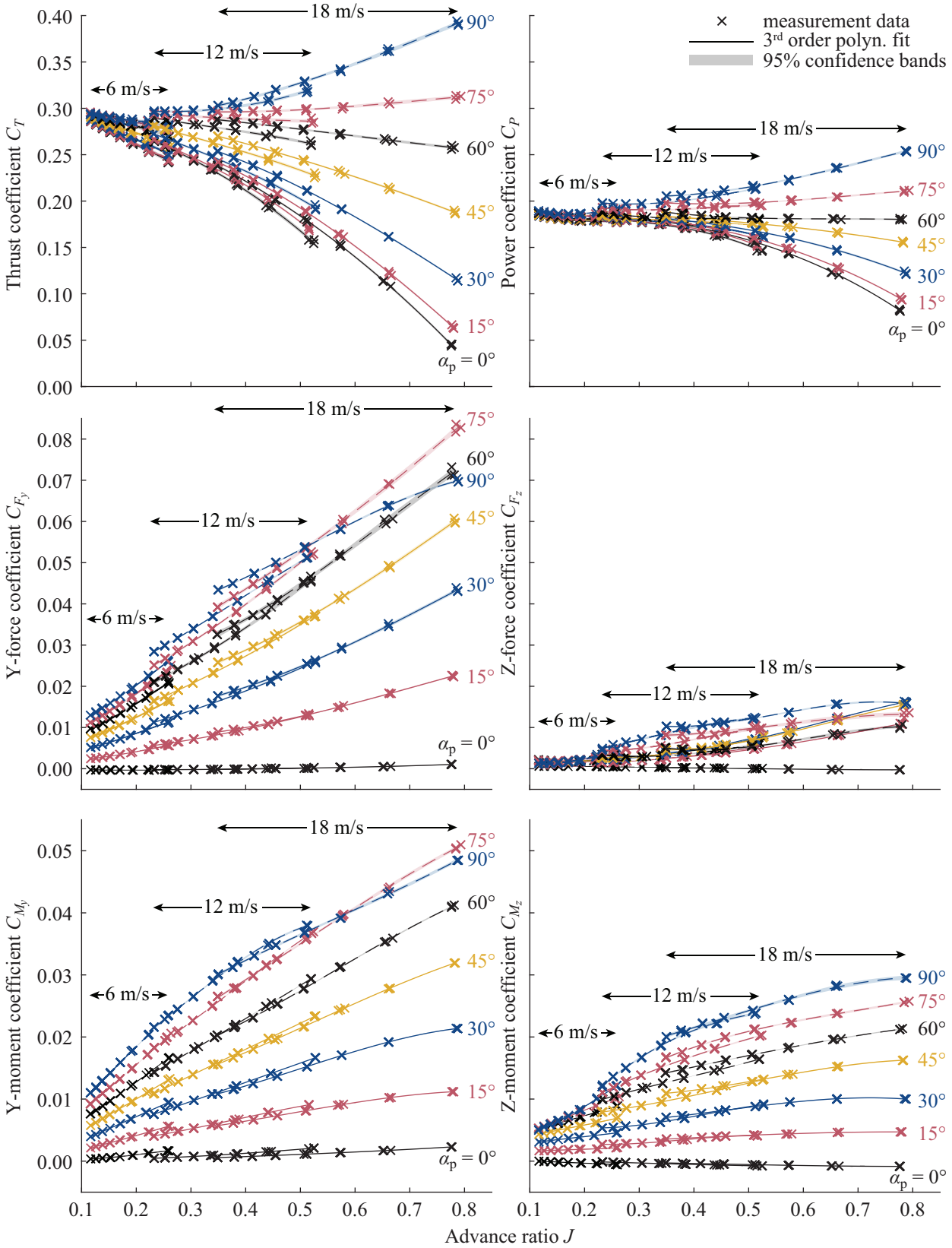

Fig. 12 Experimental result showing thrust, power, in-plane force and out-of-plane moment coefficients for $\beta_{0.7R_p}$ = 20 deg.

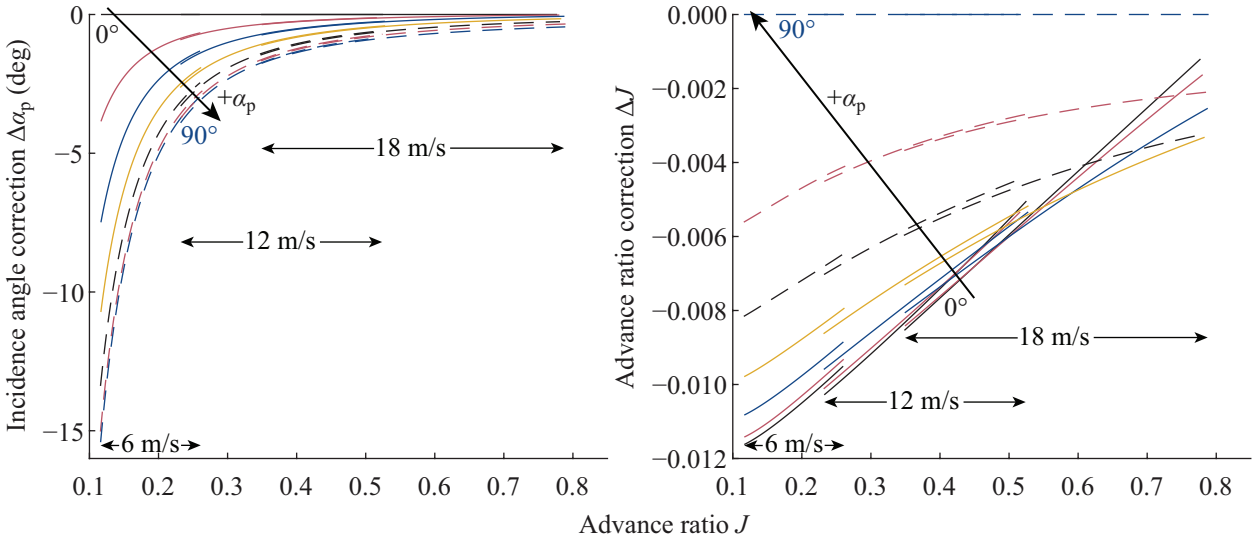

Fig. 13 Angle of attack and advance ratio wind tunnel wall corrections for the experimental results for $\beta_{0.7R_p}$ = 20 deg; linestyle and color of Fig. 12 maintained.

Not only the wind tunnel itself, also the propeller setup possibly introduces an unwanted disturbance in the performance data through the presence of the pylon. To investigate the effect of the pylon, in Fig. 14 CFD results are shown of the blade thrust evolution over the azimuth with and without presence of the pylon. Data are shown for an advance ratio of $J = 0.35$ at $V_\infty = 18$ m/s for four angles of attack. At $\alpha_p = 45$ deg the GCI uncertainty is shown to illustrate the possible uncertainty introduced by the grid. The CFD data were simulated using a transient scheme with a sliding mesh approach in the domain as presented in Fig. 6. The effect of the pylon can be noticed in the data when the blade sweeps past the pylon around $\varphi = 90$ deg. For $\alpha_p = 0$ deg there is purely an upstream pressure effect due to blockage, increasing the blade thrust by on average 0.2%. For $\alpha_p = 15$ deg and 45 deg the blade thrust is slightly increased due to the pylon by on average 0.6% and 0.7% respectively, likely caused by the increased angle of attack due to the upwash from a lift force on the pylon. At $\alpha_p = 90$ deg a small reduction in blade thrust of on average 1.1% occurs. As the pylon was normal to the flow causing considerable blockage, it might have induced a slight angle of attack reduction for the propeller.

The integrated CFD data are plotted in Fig. 15 alongside experimental data as a function of α_p for all propeller performance quantities. Results for the propeller with and without pylon effect are shown and these include the loading on the spinner. Also results with pylon effect excluding the spinner loading are presented, to show the contribution of the spinner in the performance quantities. For $\alpha_p = 45$ deg in Fig. 16 the distribution of thrust and in-plane force coefficients are plotted over the propeller disk. The corresponding time-averaged flowfield is given in Fig. 17 in terms of axial and tangential velocity, and approximated blade section angle of attack. The flowfield was obtained by time-averaging the flowfield $0.07R_p$ upstream and downstream of the propeller for a full blade passage, and taking the average of these two flowfields to obtain approximately the flowfield experienced by the propeller.

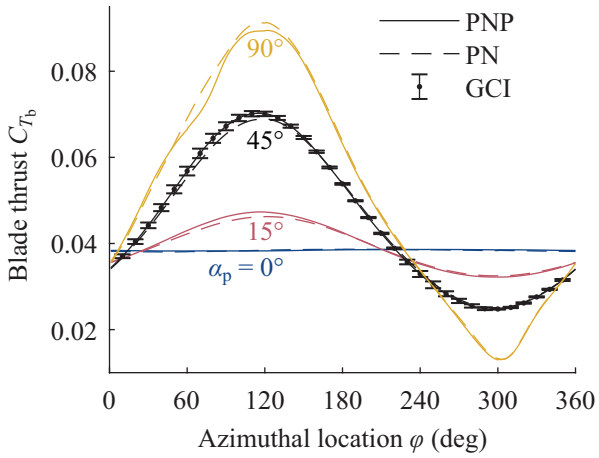

Fig. 14 CFD simulation results showing blade thrust evolution with azimuth angle with and without pylon ($\beta_{0.7R_p}$ = 20 deg, J = 0.35 and V_∞ = 18 m/s); azimuthal location φ is defined in Fig. 7.

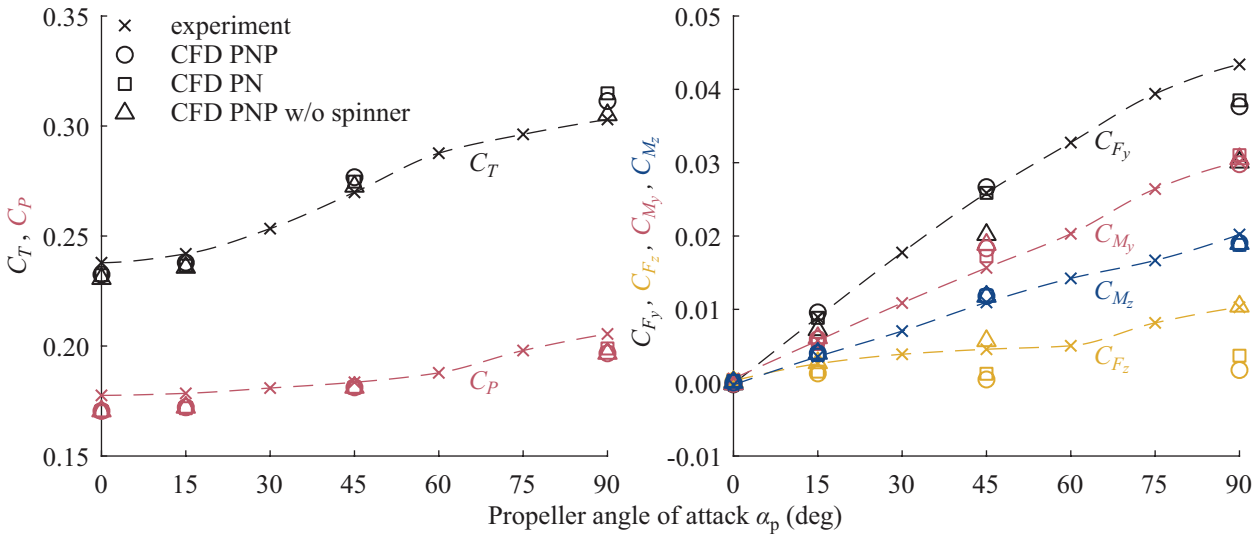

Fig. 15 Propeller performance comparison between CFD and experiment as function of α_p ($\beta_{0.7R_p}$ = 20 deg, J = 0.35 and V_∞ = 18 m/s).

The CFD predictions of thrust and power in Fig. 15 are close to the experimental values. A rise in thrust and power is seen with increasing angle of attack. In Fig. 16 a the thrust distribution is plotted as a ratio with the thrust distribution at zero angle of attack. An area of increased thrust ($c_T(r)/(c_T(r))_{\alpha_p=0} > 1$) and decreased thrust ($c_T(r)/(c_T(r))_{\alpha_p=0} < 1$) can be observed. Two effects play a role: With non-zero angle of attack, the in-plane component of the freestream, $V_\infty \sin(\alpha_p)$, results in negative and positive tangential velocity for the advancing and retreating blade side respectively (Fig. 17 b). The tangential velocity is defined positive in the rotation direction of the propeller. The negative tangential velocity results in an increase in blade section angle of attack and thus an increase in thrust and vice versa (Fig. 17 c). The second effect is that the axial component of the freestream, $V_\infty \cos(\alpha_p)$, reduces over the complete propeller disk, resulting in increased blade section angle of attack. The net effect is an increase in integrated thrust and a relatively

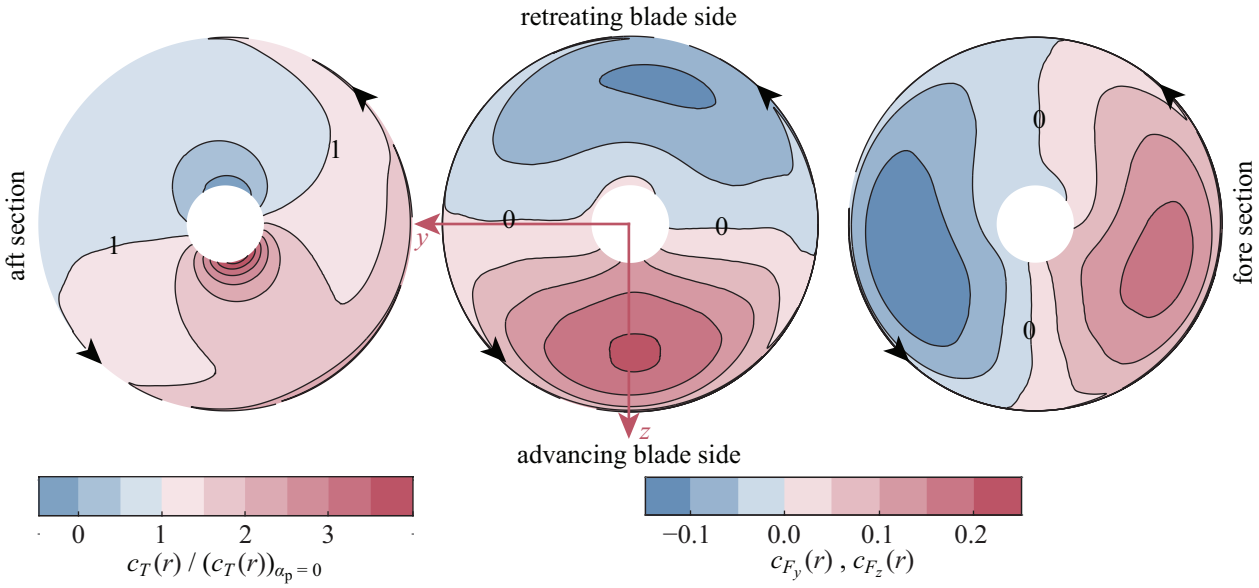

a) Relative thrust distribution. **b) *y*-force distribution.** **c) *z*-force distribution.**

Fig. 16 CFD PN result showing relative thrust and in-plane force coefficient distributions at α_p = 45 deg ($\beta_{0.7R_p}$ = 20 deg, J = 0.35 and V_∞ = 18 m/s).

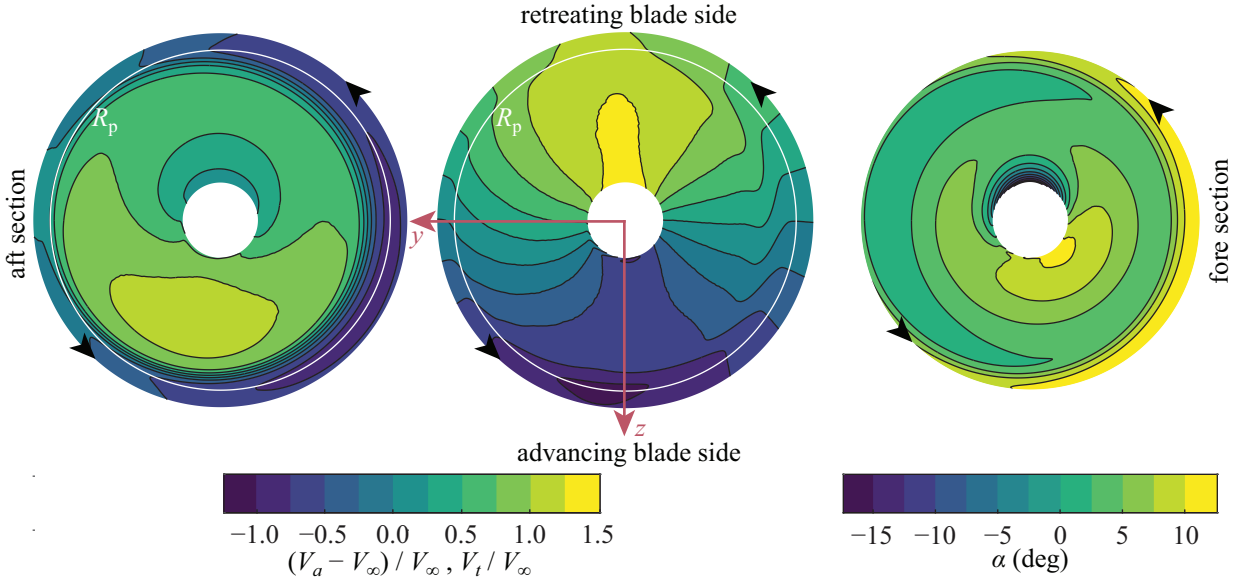

a) Axial velocity. **b) Tangential velocity.** **c) Approx. section angle of attack.**

Fig. 17 CFD PN result showing time-averaged propeller flowfield at α_p = 45 deg ($\beta_{0.7R_p}$ = 20 deg, J = 0.35 and V_∞ = 18 m/s).

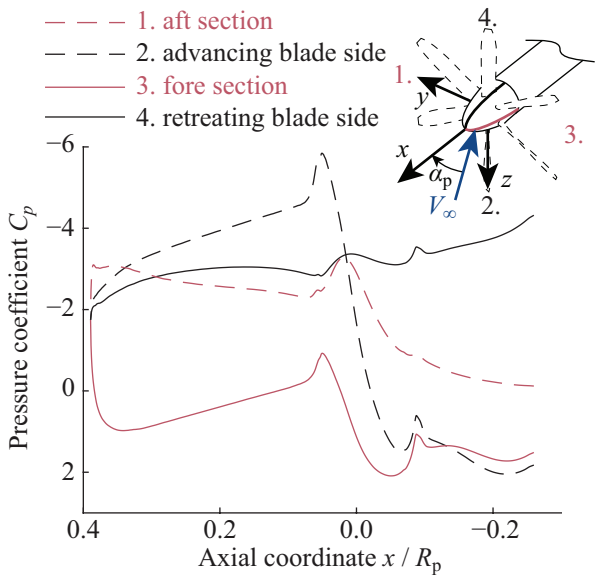

Fig. 18 CFD PN result showing the time-averaged C_p distribution on the spinner in a horizontal and vertical plane at α_p = 45 deg ($\beta_{0.7R_p}$ = 20 deg, J = 0.35 and V_∞ = 18 m/s).

smaller increase in power, resulting in an increase in thrust-over-power ratio with increasing angle of attack. The loading on the spinner only plays a minor role for the thrust and negligible role for the power.

For the largest in-plane force coefficient C_{F_y}, the CFD prediction is close to the experimental values for all propeller angles of attack except for α_p = 90 deg where a 13% under-prediction is found. C_{F_y} increases from zero to positive values with increasing angle of attack. This is because the positive contribution to C_{F_y} on the advancing blade side is larger than the negative contribution on the retreating blade side (Fig. 16 b). This imbalance in tangential force between the advancing and retreating blade side is coming from the imbalance in thrust explained in the previous paragraph. As shown in Fig. 15, at the larger angles of attack a considerable portion of C_{F_y} is formed by loading on the spinner. This is resulting from the skewed inflow to the spinner, causing a pressure difference between the fore and aft section of the propeller. To illustrate this, in Fig. 18 the time-averaged pressure coefficient distribution along the spinner is plotted along lines in the horizontal and vertical plane. Clearly, the large suction on the aft section compared to the fore section results in a net force in positive y-direction, adding to the positive y-force by the propeller blades.

The smaller in-plane force coefficient C_{F_z} is only about 20% of C_{F_y} on average. In the CFD simulations, this component is considerably underestimated. A very large part of this force component is a result of spinner loading. The part of C_{F_z} from the propeller blades results from the imbalance in tangential force between the fore and aft section, causing an area of larger positive z-force on the fore section than negative z-force on the aft section (Fig. 16 c). The larger positive z-force is caused by the phase lag in the thrust, especially for the outboard sections (Fig. 16 a). The dominant mechanism behind this phase lag are variations in induced velocity across the propeller disc as discussed by Ortun et al. [35]. On the aft section, the propeller experiences higher axial velocities and vice versa (Fig. 17 a), because

the propeller vortex system is displaced in this direction. This results in relatively larger blade section angles of attack on the fore section (Fig. 17 c) and thus in a larger thrust and tangential force component. The contribution of the spinner to C_{F_z} is a result of the higher static pressure jump on the advancing blade side than on retreating blade side from the difference in thrust [35]. In Fig. 18 the pressure coefficient distribution on the advancing and negative retreating blade side are also plotted. Upstream of the propeller, the increased suction on the advancing blade side results in a positive z-force, while downstream of the propeller the opposite occurs. The pressure difference between the advancing and retreating blade side is larger downstream of the propeller and the integrated z-force on the spinner is therefore negative, decreasing C_{F_z}. Note that the large under-prediction of C_{F_z} in the CFD simulation may be originating from the spinner loading if this pressure balance is slightly different in the experiment, although this is unclear and cannot be derived from any of the experimental or CFD results.

The prediction of the out-of-plane moment coefficients in the CFD simulations is very accurate. The spinner loading only play a minor role for these moment components. Both components increase with increasing α_p. The positive values for C_{M_y} are resulting from the imbalance in thrust distribution between the advancing and retreating blade side as plotted in Fig. 16 a. Likewise, the positive values for C_{M_z} originate from the imbalance in thrust distribution between the fore and aft section.

V. Results with Wing Interaction

In this part, propeller performance results with wing interaction are discussed. This section deals with simulating the effect of main rotor downwash on the propeller-wing assembly in hover mode. The situation in the experiment is sketched in Fig. 19. The wind tunnel jet impinged at $\alpha_\mathrm{p} = 90$ deg, normal to the wing planform. When the propeller was off, a stagnation line formed over the upper side of the wing and flow separation occurred around the leading and trailing edges and the wingtip. Approximated shearlines from tuft visualization are presented in Fig. 20. These highlight the stagnation line at approximately two-thirds of the chord from the leading edge. The figure shows that the shearline pattern changes under the influence of the propeller as the propeller draws in air. On the outboard sections of the wing the stagnation line moves toward the leading edge.

As the propeller influences the flow around the wing, the opposite also occurs. The inflow to the propeller is affected, resulting in modified propeller performance. The effect that the wing has on the propeller performance is discussed in the next Section V.A. As shown in Fig. 19, the chordwise distance of the wing to the propeller d_w was varied in the experiment, as well as the flap deflection δ_f. This was done to parametrically study the interaction effect of the wing. In Section V.B, these experimentally obtained interaction effects on the propeller performance are discussed. Performance changes of the wing are not discussed as the wing was not instrumented. Therefore, the presented results are not necessarily representative for the complete design as the propeller performance changes may be different from the system performance changes.

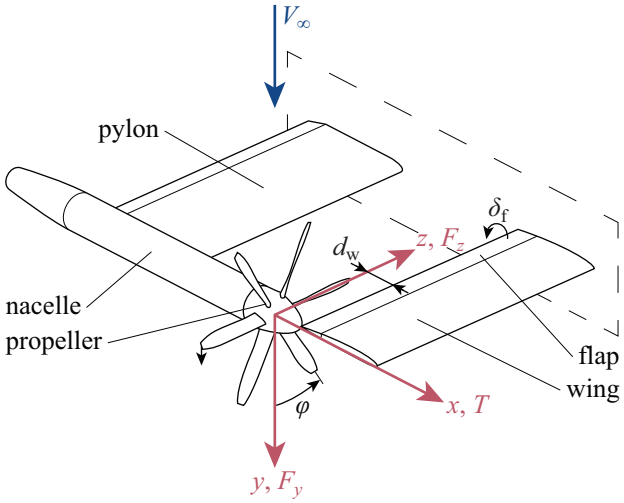

Fig. 19 Sketch of propeller setup with wing, including definition of wing distance d_w, flap deflection δ_f, blade phase angle φ, and force components.

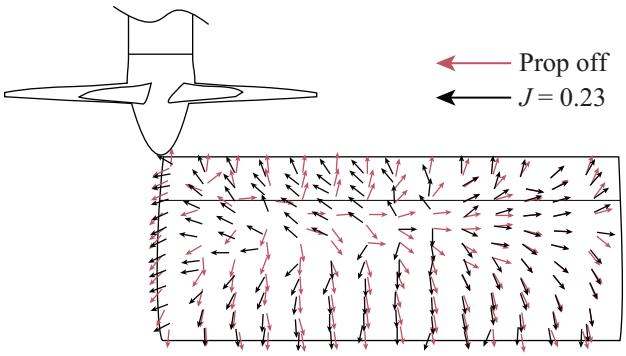

Fig. 20 Flow visualization on wing based on experimental measurement with tufts ($\beta_{0.7R_p}$ = 20 deg, V_∞ = 12 m/s, d_w/R_p = 0.4 and δ_f = 0 deg); view along the direction of tunnel flow.

While the goal of the experiment was to study the effect of the wing on the propeller performance, also possible unwanted interaction from the pylon was present. The effect of the pylon on the interaction results was studied with CFD RANS simulations and results are presented in Section V.C. Furthermore, as the experiment should represent interaction for a compound helicopter in hover, main rotor flow was approximated with a non-uniform actuator-disk in the CFD simulations and compared to the situation with uniform freestream flow. The actuator-disk introduces the time-averaged effect of the main rotor on the flowfield, including the radial non-uniformity present in the hover condition. However, any of the transient effects that the main rotor blade tip vortices and wakes have on the propeller are not present, as well as any effect that the propeller has on the main rotor loading.

A. Propeller Performance with Wing

All results in this section were obtained for a fixed wing position and flap deflection of $d_w/R_p = 0.4$ and $\delta_f = 0$ deg, while in the next section these are varied. In Fig. 21 the main experimental performance results with wing are plotted

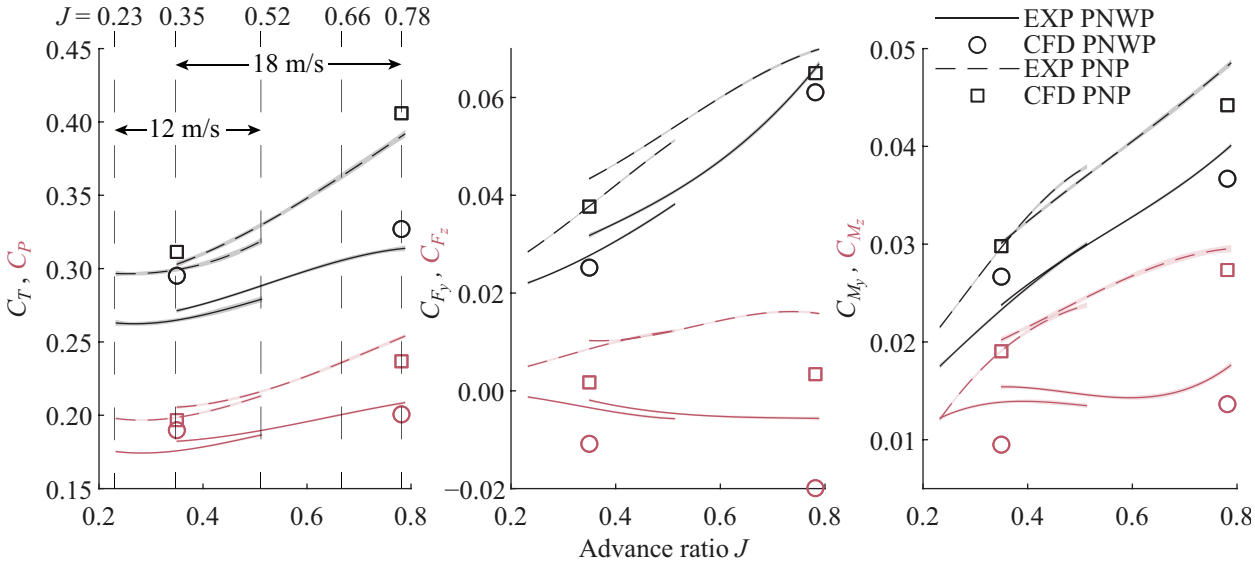

Fig. 21 Propeller performance with and without wing effect ($\beta_{0.7R_p}$ = 20 deg, d_w/R_p = 0.4 and δ_f = 0 deg); CFD simulations obtained at 18 m/s.

versus advance ratio as 3rd order polynomial fits of the experimental data with 95% simultaneous confidence bands. As a reference, also the performance without wing at α_p = 90 deg is given and CFD results of the same configurations for J = 0.35 and J = 0.78 at 18 m/s are shown too. The wing causes a reduction of thrust and power, in-plane forces and out-of-plane moments. The results with wing show some similarity to those without wing at reduced angle of attack ($\alpha_p \approx 60 - 75$ deg) from Fig. 12. The CFD simulations also predict reductions in the performance quantities, although with considerable error compared to the experiment. This is partly due to a discrepancy in the prediction without wing at α_p = 90 deg as discussed in relation to Fig. 15 and partly due to a discrepancy in the prediction of the effect of the wing. It is thought that, despite the differences, the mechanism of the aerodynamic interaction can be investigated with the CFD simulation results.

A comparison of the blade thrust evolution with and without wing in Fig. 22 a highlights where the differences arise. As visualized in Fig. 23, for $-30 < \varphi < 60$ deg (region A.) the propeller blade draws low momentum air from a wake formed below the wing. Flowfield analysis similar to that for Fig. 17 reveals the approximated blade section angle of attack in Fig. 22 b. As the propeller blade operates in somewhat static condition in this area, the section angle of attack is larger than when no wing is present. As a result of this, the thrust is larger too. When the blade reaches the vicinity of the trailing edge of the wing at φ = 90 deg, a decreased thrust due to the wing is found. The wing acts as a guiding vane, decreasing the large angle of attack of the freestream flow and locally increasing the axial velocity component in the propeller reference frame. As a result, the blade section angle of attack for $60 < \varphi < 180$ deg (region B.) is relatively small compared to the situation without wing and thus the corresponding thrust is reduced too. In the remainder of the blade evolution (region C.), the thrust is very similar and no large influence of the wing is found. The

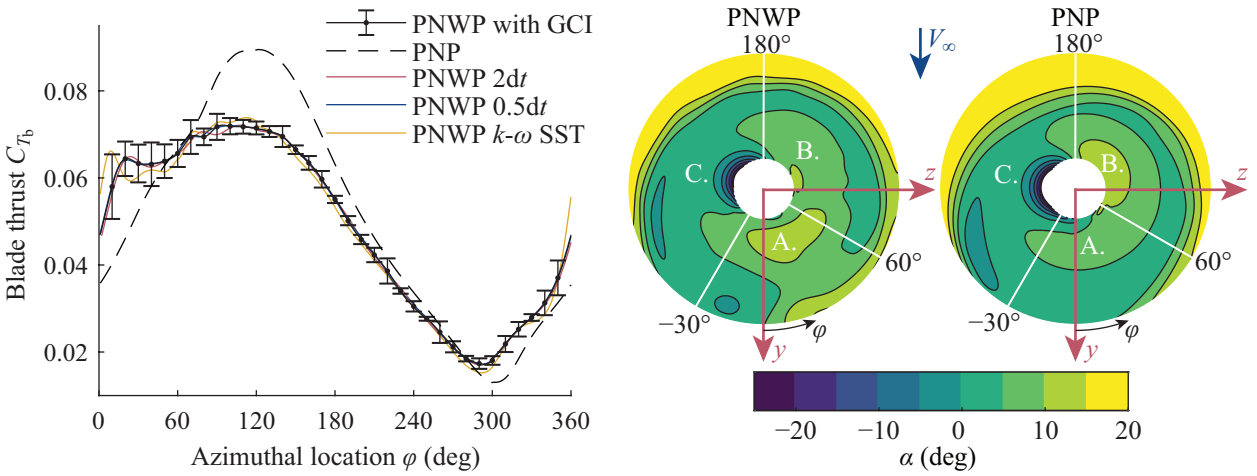

a) Blade thrust evolution. **b) Approximated blade section angle of attack.**

Fig. 22 CFD results showing blade thrust evolution and section approximated angle of attack with and without wing effect ($\beta_{0.7R_p}$ = 20 deg, J = 0.35, V_∞ = 18 m/s, d_w/R_p = 0.4 and δ_f = 0 deg); includes effect of timestep and tubulence model.

net result is a decrease of thrust.

A similar interaction with the wing was found for the left propeller on the compound helicopter in Fig. 1 a as described in Ref. [11]. However, the increase in thrust in region A. was found to be larger than the decrease of thrust in region B. and thus a net thrust increase as a result of the wing was found for the compound helicopter. Although the results of Frey et al. [13] show that also for this compound helicopter the wing can cause a net decrease of thrust.

Also a decrease of C_P as a result of the wing is shown in Fig. 21, which can be explained with same mechanism as described for C_T. The in-plane force coefficients decrease as well due to wing interaction. This is a result of changes to the in-plane tangential force on the propeller blade sections. As the thrust in region A. (See Fig. 22 b) is increased due to the wing, also an increase in the tangential force occurs. This results in a decrease in force in z-direction and thus C_{F_z} decreases. As the thrust in region B. is decreased due to the wing, the accompanying decrease in tangential force results in a decrease in force in y-direction and thus C_{F_y} decreases. The out-of-plane moment coefficients follow similar trends due to the local changes in thrust.

The PNWP configuration is the most complex configuration in terms of aerodynamic interaction phenomena. Therefore, the chosen timestep and turbulence model were evaluated for this configuration. In Fig. 22 a the blade thrust evolution is shown for the PNWP configuration with a timestep equivalent to 0.5 deg and 2 deg of propeller rotation alongside the PNWP results with the default timestep equivalent to 1 deg of propeller rotation. Furthermore, results with the two-equation eddy viscosity $k-\omega$ SST turbulence model are shown with default timestep. In terms of timestep, only very small differences can be noticed, so the default timestep is considered sufficiently small. The result with the $k-\omega$ SST turbulence model shows only small deviations from the default result with the Spalart–Allmaras turbulence model, despite the formation of the large wake behind the wing.

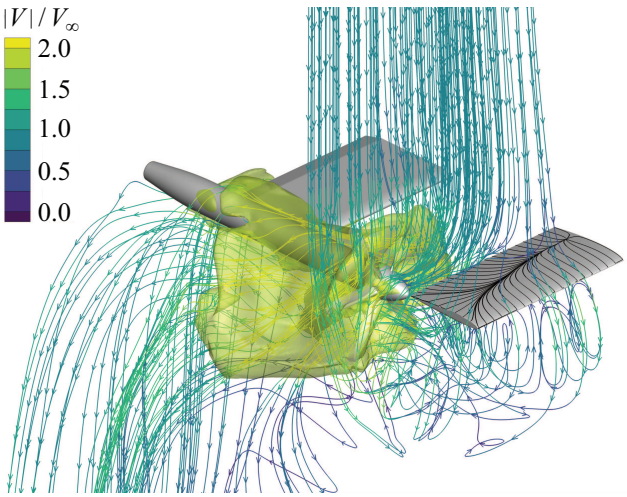

Fig. 23 CFD PNWP result of wing interaction ($\beta_{0.7R_p}$ = 20 deg, J = 0.35, V_∞ = 18 m/s, d_w/R_p = 0.4 and δ_f = 0 deg); includes streamtraces with contour of velocity magnitude, isosurface for $|V|/V_\infty$ = 2, and shearlines on wing (black).

B. Effect of Wing Position and Flap Deflection

The effect of the wing with varying wing position is presented in Fig. 24 as the ratio of thrust coefficient and thrust-over-power ratio with wing to the same quantities without wing. Results are shown for four advance ratios with V_∞ = 12 m/s and 18 m/s. For the closest distance of d_w/R_p = 0.4, the wing results in a clear thrust lapse as explained in the previous section. This is especially the case for the higher advance ratios as the propeller becomes relatively more sensitive to inflow changes when the rotational speed is lower, resulting in a maximum thrust reduction of 20% for J = 0.78. This dependency on J was already seen for the isolated propeller performance, where the effect of angle of attack in Fig. 12 was found to be larger for higher J.

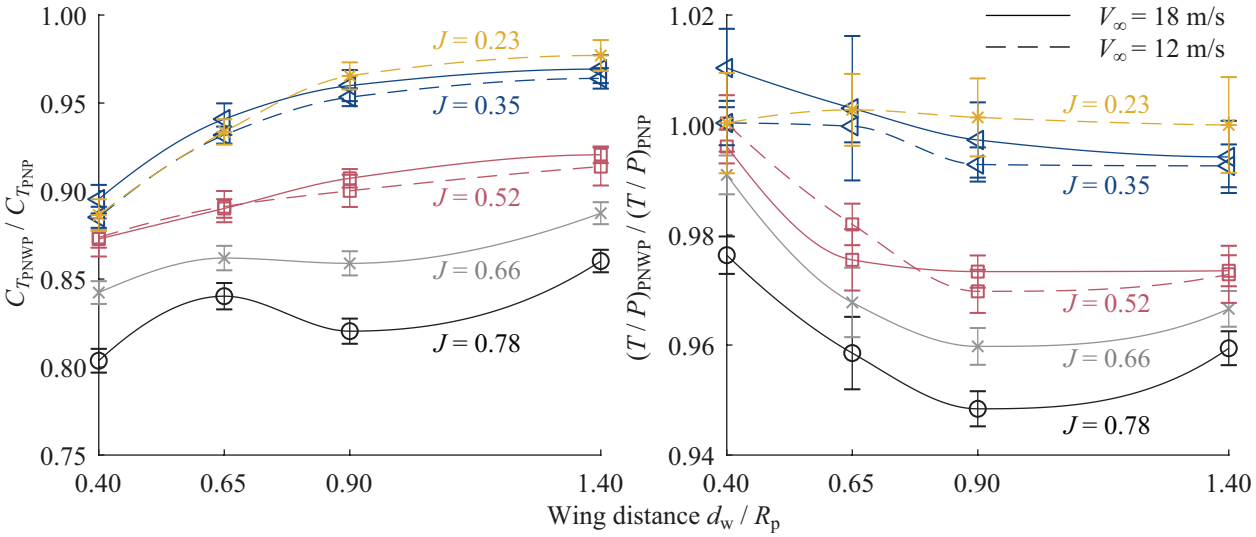

Fig. 24 Experimental result showing change in propeller loading due to wing versus wing distance ($\beta_{0.7R_p}$ = 20 deg and δ_f = 0 deg).

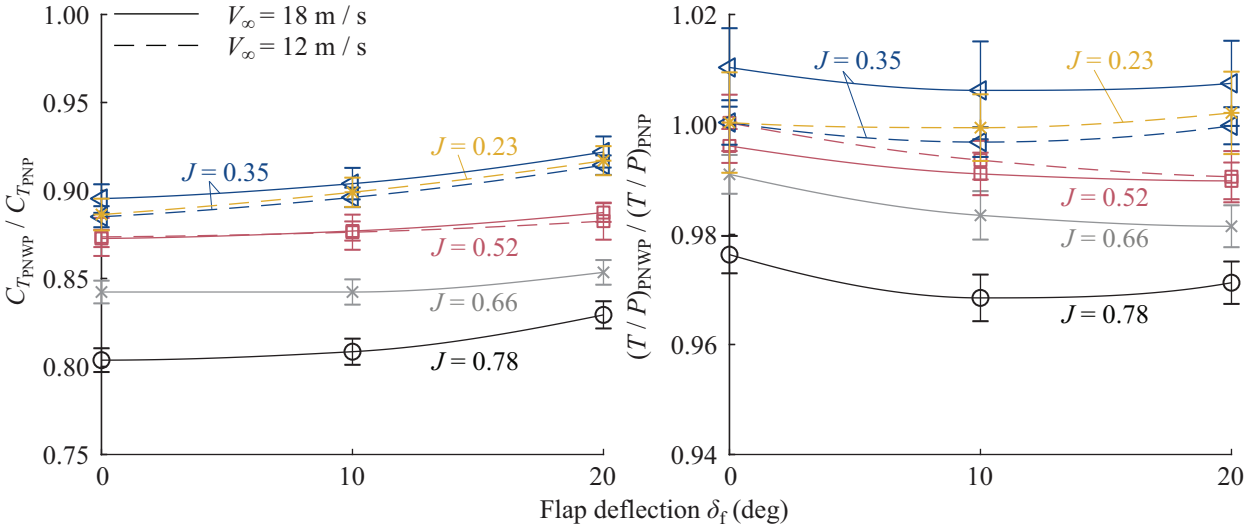

Fig. 25 Experimental result showing change in propeller loading due to wing versus flap deflection ($\beta_{0.7R_p}$ = 20 deg and $d_w/R_p = 0.4$).

When the wing distance increases, the thrust increases, except for the higher advance ratios ($J = 0.78$ and to a lesser extent $J = 0.66$) where an intermediate reduction is found for $d_w/R_p = 0.9$. From the data available it is unclear what the cause is of this intermediate reduction in thrust, but it is most likely a physical effect as it is seen in repeated measurements for two different J and the effect gradually disappears with decreasing J. Note that, while the relative changes in thrust are large for higher advance ratios, the absolute changes are small as the loading is relatively low for these operating conditions.

The thrust-over-power ratio T/P indicates the efficiency of the propeller operation. Depending on J, the wing either leads to a small increase or decrease of T/P. With increasing wing distance, the T/P ratio generally reduces. Apparently the disturbance of the inflow by the wing is for most tested operating conditions disadvantageous for the propeller performance. A similar conclusion was reached for the left propeller on the compound helicopter in Fig. 1 a. as described in Ref. [11].

The effects of flap deflection on the propeller performance are presented in Fig. 25. Compared to wing distance, only minor variations of the propeller performance quantities with flap deflection are found. If one would want to alleviate the effects of the wing on the propeller performance, increasing the distance seems more effective. Although possibly larger flap deflections could be tried to see if the trend of reducing wing effect continues.

C. Effect of Pylon and Main Rotor Flow

In this section the presence of the pylon is investigated for the cases with wing by means of CFD simulations. Furthermore, the freestream flow is changed to a time-averaged approximation of main rotor flow by means of a non-uniform actuator-disk (AD), to investigate how representative the experimental data is for the interaction on the

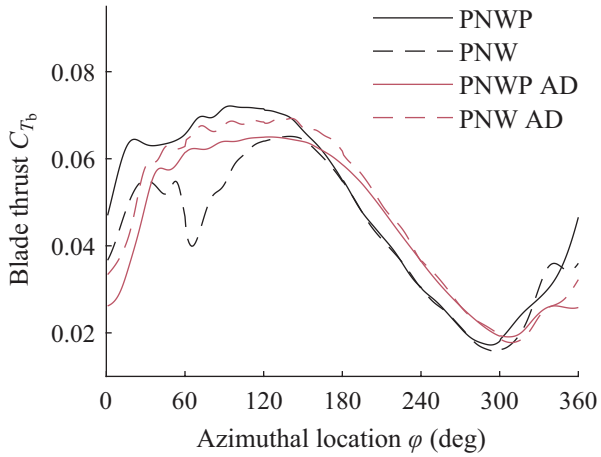

Fig. 26 CFD blade thrust evolution showing effect of pylon and non-uniform actuator-disk modeling ($\beta_{0.7R_p}$ = 20 deg, J = 0.35, V_∞ = 18 m/s, d_w/R_p = 0.4 and δ_f = 0 deg); azimuthal location φ is defined in Fig. 19.

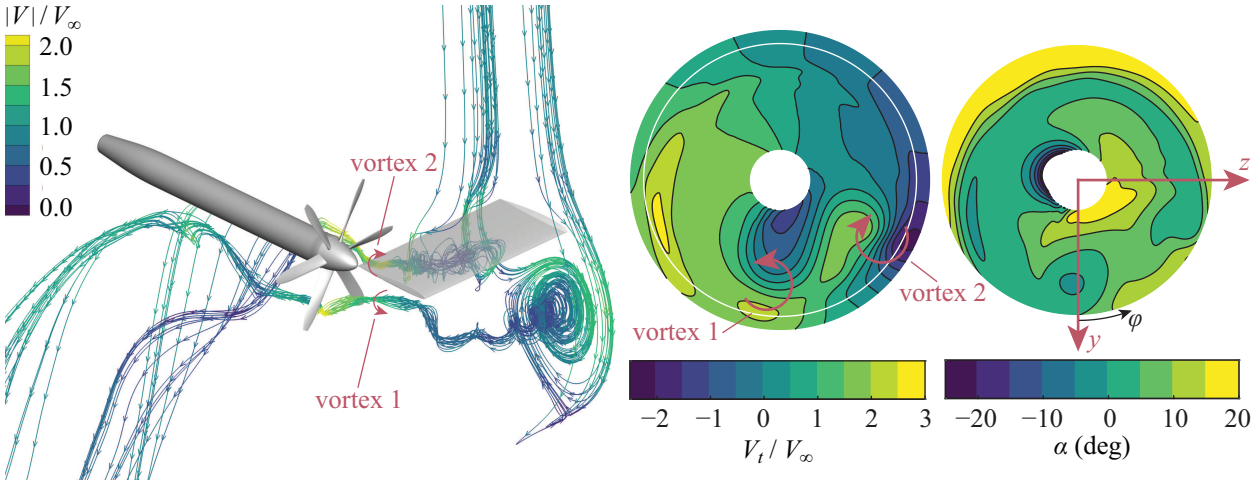

a) Visualization of vortex pair ingested by propeller. **b) Corresponding time-averaged propeller flowfield.**

Fig. 27 CFD visualization of vortex pair and contours of propeller flowfield for PNW configuration ($\beta_{0.7R_p}$ = 20 deg, J = 0.35, V_∞ = 18 m/s, d_w/R_p = 0.4 and δ_f = 0 deg).

compound helicopter. In Fig. 26 the blade thrust evolution is shown for all CFD configurations with wing. First consider the data with freestream flow. With the wing present, the effect of the pylon on the propeller thrust is not small, unlike for the case without wing where changes in thrust in the order of 1% were found. The pylon reduces the time-averaged thrust by 11.5% according to the simulations.

In Fig. 27 the flowfield experienced by the propeller is presented for the case without pylon. In Fig. 27 a, a vortex pair can be observed from the streamtraces (checked with vorticity isosurfaces), which is formed in the wake of the wing. Apparently, the formation of these vortices is suppressed when the pylon is present, likely due to changes in the inflow direction to the wing induced by the pylon. This vortex pair is ingested by the propeller and has a significant effect on the propeller loading. In Fig. 27 b the consequence of the vortex pair on the flowfield experienced by the propeller is shown.

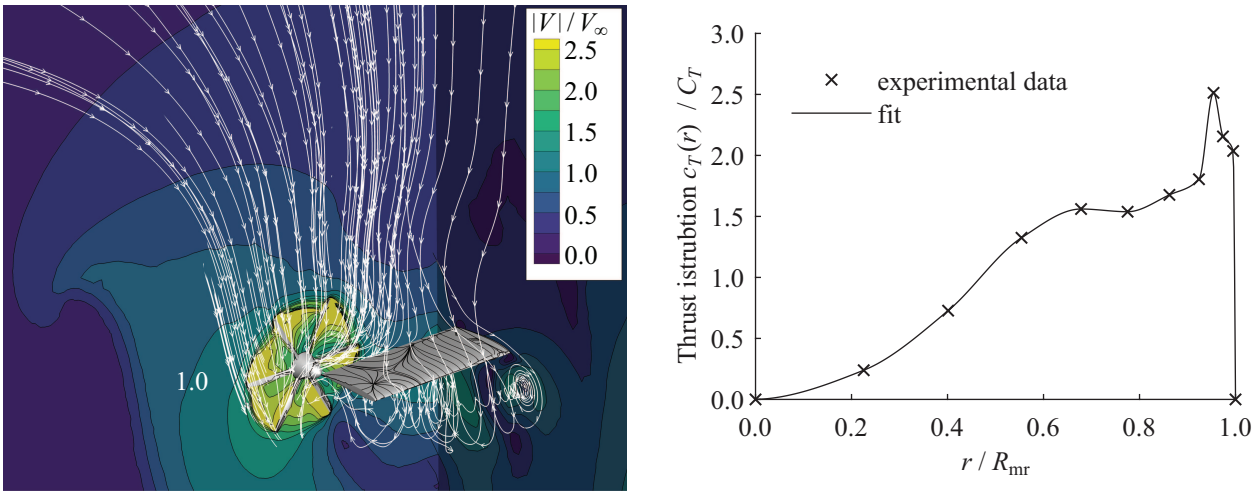

a) Flowfield of propeller and wing with actuator disk. **b) Assumed main rotor radial thrust distribution.**

Fig. 28 CFD visualization of flowfield with main rotor modeling and corresponding thrust distribution ($\beta_{0.7R_p}$ = 20 deg, J = 0.35, V_∞ = 18 m/s, d_w/R_p = 0.4 and δ_f = 0 deg); includes streamtraces (white) and shearlines on wing (black).

In the tangential velocity field, the effect of the vortices is seen by two areas of increased and decreased V_t. This has a pronounced effect on the section angle of attack. Vortex 1, located around $\varphi = 0$ deg, results in increased α near the root of the blade and decreased α near the tip. As the loading on the propeller blade generally increases towards the tip with maxima outboard of $r/R_p = 0.8$ (see Fig. 10), the impact of the reduction in α is larger and a thrust reduction is found around $\varphi = 0$ deg in Fig. 26. As vortex 2 is of opposite sign to vortex 1 and is located radially more outboard, also this vortex results in a pronounced reduction of thrust, visible in Fig. 26 by the local minimum around $\varphi = 60$ deg. For the remainder of the blade evolution, no significant differences in blade thrust are found due to the pylon. As a vortex pair of such strength is only present for the PNW configuration and not for the other CFD configurations with wing (PNWP, PNWP AD and PNW AD), it is unclear whether this would occur in the experiment if the pylon was removed.

Fig. 26 also includes results where the freestream flow was replaced by flow induced by a non-uniform actuator-disk representing the time-averaged effect of a main rotor. For the case with pylon, qualitatively a similar thrust distribution is found, but a phase shift is present. The mean thrust is decreased by 7.0% as a result of the simulated main rotor downwash. When the actuator-disk is present, the effect of the pylon on the thrust distribution is less pronounced. In Fig. 28 a the actuator-disk flowfield is visualized while in Fig. 28 b the assumed main rotor radial thrust distribution is shown. Considering the large radial non-uniformity of the oncoming flow as a result of the non-uniformity in main rotor thrust distribution, the effects this has on the propeller thrust distribution is surprisingly small. Because of this similarity in thrust evolution, it is thought that the conclusions as drawn in the previous two sections based on the experimental results with freestream flow, are representative for the interaction occurring on the compound helicopter. However, the aspect missing in this interaction are the unsteady effects of the main rotor flow on the propeller performance.

VI. Conclusion

An experimental dataset was presented of propeller performance in static condition and at low subsonic airspeeds for various angles of attack up to 90 deg. The propeller loading was described in terms of thrust, power, in-plane forces and out-of-plane moments. The CFD RANS model was found to be consistent with the experimental dataset of the same configuration as long as major flow separation on the blades was prevented by selection of an appropriate blade pitch angle. To mount the propeller, a pylon was present in its slipstream. A numerical investigation showed that the effect of the pylon on the propeller performance was small, in the order of 1% for the thrust for various angles of attack. Also wind tunnel wall corrections were investigated for the experimental data. It is concluded that this experimental dataset is free of major errors and is very suitable for validation of propeller models for e.g. research on eVTOL vehicles or compound helicopters where propellers experience large angles of attack.

At an angle of attack of 90 deg the interaction of the propeller with an upstream wing was studied. The wing was found to reduce all propeller performance quantities on average. In terms of thrust, a thrust increasing and thrust decreasing mechanism were found numerically, leading to a net thrust decrease. A local blade thrust increase of up to 35% of the time average arose as the propeller drew air from the low momentum wake formed on one side of the wing. A local thrust decrease of up to 35% of the time average occurred because the wing acted as a turning vane for the freestream flow, locally decreasing the angle of attack and increasing the axial velocity component in the inflow to the propeller. Wing distance and flap deflection were varied in the experiment. For the closest distance to the propeller, a maximum thrust decrease of 20% was found for the highest tested advance ratio. For most tested operating conditions, the wing resulted in a small decrease of propeller thrust-over-power ratio in the order of 1%. With decreasing advance ratio and increasing wing distance, the effect of the wing on on thrust and power generally decreased. For the tested range from 0 deg to 20 deg, flap deflection had only a minor influence on the propeller performance, decreasing the effect of the wing slightly.

From the numerical investigation of the effect of the pylon on the propeller performance it was found that it may have been significant (11.5% thrust reduction) as the inflow to the wing was influenced. A pair of strong vortices in the wake of the wing were discovered to be the source of the performance change. It is unknown whether in the experiment a similar phenomenon would have occurred without pylon. As wing interaction was studied to represent the interaction occurring for the left propeller on the compound helicopter in hover, the freestream flow in the CFD simulation was also replaced with the time-averaged effect of a main rotor through a non-uniform actuator-disk. Despite the non-uniform velocity distribution in the main rotor slipstream, no major changes in blade thrust evolution were found compared to the situation with freestream flow. With the actuator-disk no strong vortex pair was formed in the wing wake when the pylon was removed, suggesting that this phenomenon is very particular to the exact configuration and operating condition. In general, the results in this study are qualitatively representative for the aerodynamic interaction occurring on the compound helicopter in hover.

Acknowledgments

The authors would like to thank Tomas Sinnige, Assistant Professor in the Flight Performance and Propulsion section, and Nando van Arnhem, Ph.D. candidate in the Flight Performance and Propulsion section, for their technical support during the wind-tunnel campaign.

References

[1] Whitlow, J. B., and Sievers, G. K., "Fuel Savings Potential of the NASA Advanced Turboprop Program," Technical Memorandum 83736, NASA, Cleveland, Ohio, Sep. 1984.

[2] Kim, H. D., Perry, A. T., and Ansell, P. J., "A Review of Distributed Electric Propulsion Concepts for Air Vehicle Technology," *2018 AIAA/IEEE Electric Aircraft Technologies Symposium*, AIAA Paper 2018-4998, Cincinnati, Ohio, 2018. doi:10.2514/6.2018-4998.

[3] Kasliwal, A., Furbush, N. J., Gawron, J. H., McBride, J. R., Wallington, T. J., Kleine, R. D. D., Kim, H. C., and Keoleian, G. A., "Role of Flying Cars in Sustainable Mobility," *Nature Communications*, Vol. 10, No. 1, 2019, pp. 1–9. doi:10.1038/s41467-019-09426-0.

[4] Johnson, W., Silva, C., and Solis, E., "Concept Vehicles for VTOL Air Taxi Operations," *AHS Technical Conference on Aeromechanics Design for Transformative Vertical Flight*, San Francisco, California, 2018.

[5] Silva, C., Johnson, W. R., Solis, E., Patterson, M. D., and Antcliff, K. R., "VTOL Urban Air Mobility Concept Vehicles for Technology Development," *2018 Aviation Technology, Integration, and Operations Conference*, AIAA Paper 2018-3847, Atlanta, Georgia, 2018. doi:10.2514/6.2018-3847.

[6] Kraenzler, M., Schmitt, M., and Stumpf, E., "Conceptual Design Study on Electrical Vertical Take Off and Landing Aircraft for Urban Air Mobility Applications," *AIAA Aviation 2019 Forum*, AIAA Paper 2019-3124, Dallas, Texas, 2019. doi:10.2514/6.2019-3124.

[7] Lienard, C., Salah el Din, I., Renaud, T., and Fukari, R., "RACER High-Speed Demonstrator: Rotor and Rotor-Head Wake Interactions with Tail Unit," *AHS International 74th Annual Forum & Technology Display*, Phoenix, Arizona, 2018.

[8] Stokkermans, T. C. A., Voskuijl, M., Veldhuis, L. L. M., Soemarwoto, B., Fukari, R., and Eglin, P., "Aerodynamic Installation Effects of Lateral Rotors on a Novel Compound Helicopter Configuration," *AHS International 74th Annual Forum & Technology Display*, Phoenix, Arizona, 2018.

[9] Wentrup, M., Yin, J., Kunze, P., Streit, T., Wendisch, J.-H., Schwarz, T., Pinacho, J.-P., Kicker, K., and Fukari, R., "An Overview of DLR Compound Rotorcraft Aerodynamics and Aeroacoustics Activities within the CleanSky2 NACOR Project," *AHS International 74th Annual Forum & Technology Display*, Phoenix, Arizona, 2018.

[10] Thiemeier, J., Öhrle, C., Frey, F., Keßler, M., and Krämer, E., "Aerodynamics and Flight Mechanics Analysis of Airbus Helicopters' Compound Helicopter RACER in Hover under Crosswind Conditions," *CEAS Aeronautical Journal*, Vol. 11, 2020, pp. 49–66. doi:10.1007/s13272-019-00392-3.

[11] Stokkermans, T., Veldhuis, L., Soemarwoto, B., Fukari, R., and Eglin, P., "Breakdown of Aerodynamic Interactions for the Lateral Rotors on a Compound Helicopter," *Aerospace Science and Technology*, Vol. 101, 2020, p. 105845. doi: 10.1016/j.ast.2020.105845.

[12] Frey, F., Thiemeier, J., Öhrle, C., Keβler, M., and Krämer, E., "Aerodynamic Interactions on Airbus Helicopters' Compound Helicopter RACER in Cruise Flight," *Journal of the American Helicopter Society*, Vol. 65, No. 4, 2020, pp. 1–14. doi: 10.4050/JAHS.65.042001.

[13] Frey, F., Öhrle, C., Thiemeier, J., Keßler, M., and Krämer, E., "Aerodynamic Interactions on Airbus Helicopters' Compound Helicopter RACER in Hover," *VFS International 76th Annual Forum & Technology Display*, Virginia Beach, Virginia, 2020.

[14] Yeo, H., and Johnson, W., "Optimum Design of a Compound Helicopter," *Journal of Aircraft*, Vol. 46, No. 4, 2009, pp. 1210–1221. doi:10.2514/1.40101.

[15] Enconniere, J., Ortiz-Carretero, J., and Pachidis, V., "Mission Performance Analysis of a Conceptual Coaxial Rotorcraft for Air Taxi Applications," *Aerospace Science and Technology*, Vol. 69, 2017, pp. 1–14. doi:10.1016/j.ast.2017.06.015.

[16] Patterson Jr, J. C., and Bartlett, G. R., "Effect of a Wing-Tip Mounted Pusher Turboprop on the Aerodynamic Characteristics of a Semi-Span Wing," *AIAA/SAE/ASME/ASEE 21st Joint Propulsion Conference*, AIAA Paper 1985-1286, Monterey, California, 1985. doi:10.2514/6.1985-1286.

[17] Janus, J. M., Chatterjee, A., and Cave, C., "Computational Analysis of a Wingtip-Mounted Pusher Turboprop," *Journal of Aircraft*, Vol. 33, No. 2, 1996, pp. 441–444. doi:10.2514/3.46959.

[18] Miranda, L. R., and Brennan, J. E., "Aerodynamic Effects of Wingtip-Mounted Propellers and Turbines," *4th Applied Aerodynamics Conference*, AIAA Paper 1986-1802, San Diego, California, 1986. doi:10.2514/6.1986-1802.

[19] Stokkermans, T. C. A., Nootebos, S., and Veldhuis, L. L. M., "Analysis and Design of a Small-Scale Wingtip-Mounted Pusher Propeller," *AIAA Aviation 2019 Forum*, AIAA Paper 2019-3693, Dallas, Texas, 2019. doi:10.2514/6.2019-3693.

[20] McLemore, H. C., and Cannon, M. D., "Aerodynamic Investigation of a Four-Blade Propeller Operating Through an Angle-of-Attack Range from 0 Deg to 180 Deg," Technical Note 3228, NACA, Langley Field, Virginia, Jun. 1954.

[21] Smith, H. R., "Engineering Models of Aircraft Propellers at Incidence," Dissertation, University of Glasgow, Glasgow, United Kingdom, 2015.

[22] Droandi, G., Gibertini, G., Grassi, D., Campanardi, G., and Liprino, C., "Proprotor–Wing Aerodynamic Interaction in the First Stages of Conversion from Helicopter to Aeroplane Mode," *Aerospace Science and Technology*, Vol. 58, 2016, pp. 116–133. doi:10.1016/j.ast.2016.08.013.

[23] Li, Q., Öztürk, K., Sinnige, T., Ragni, D., Eitelberg, G., Veldhuis, L., and Wang, Y., "Design and Experimental Validation of Swirl-Recovery Vanes for Propeller Propulsion Systems," *AIAA Journal*, Vol. 56, No. 12, 2018, pp. 4719–4729. doi: 10.2514/1.J057113.

[24] Li, Q., Liu, X., Eitelberg, G., and Veldhuis, L., "Numerical Investigation of Configurations with Optimum Swirl Recovery for Propeller Propulsion Systems," *AIAA Journal*, Vol. 57, No. 4, 2019, pp. 1502–1513. doi:10.2514/1.J057704.

[25] Nahuis, R., and Sinnige, T., "Design, Manufacture and Commissioning of a New NLR Six-Component Rotating Shaft Balance for Delft University of Technology," *10th International Symposium on Strain-Gauge Balances*, Mianyang, China: China Aerodynamics Research and Development Center, 2016.

[26] Sayers, A. T., and Ball, D. R., "Blockage Corrections for Rectangular Flat Plates Mounted in an Open Jet Wind Tunnel," *Proceedings of the Institution of Mechanical Engineers, Part C: Journal of Mechanical Engineering Science*, Vol. 197, No. 4, 1983, pp. 259–263. doi:10.1243/PIME_PROC_1983_197_107_02.

[27] Hackett, J. E., Ashill, P. R., and Mokry, M., "Wall Correction Methods for Powered Models of Conventional Take Off and Landing Aircraft," AGARDograph 336, Advisory Group for Aerospace Research and Development, Neuilly-Sur-Seine, France, Oct. 1998.

[28] Langer, H.-J., Peterson, R. L., and Maier, T. H., "An Experimental Evaluation of Wind Tunnel Wall Correction Methods for Helicopter Performance," *AHS International Forum 52*, Washington, D.C., 1996.

[29] Barlow, J. B., Rae, W. H., and Pope, A., *Low-Speed Wind Tunnel Testing*, 3rd ed., Wiley-Interscience, New York, 1999.

[30] Serrano, D., Ren, M., Qureshi, A. J., and Ghaemi, S., "Effect of Disk Angle-of-Attack on Aerodynamic Performance of Small Propellers," *Aerospace Science and Technology*, Vol. 92, 2019, pp. 901–914. doi:10.1016/j.ast.2019.07.022.

[31] Anon, "Help System ANSYS® Academic Research Release 18.1, Fluent," ANSYS, Inc., Software, 2017.

[32] Anon, "U.S. Standard Atmosphere, 1976," Tech. Rep. NOAA-S/T 76-1562, NOAA, NASA, US Air Force, Washington, D.C., Oct. 1976.

[33] Barth, T., and Jespersen, D., "The Design and Application of Upwind Schemes on Unstructured Meshes," *27th Aerospace Sciences Meeting*, AIAA Paper 1989-366, Reno, Nevada, 1989. doi:10.2514/6.1989-366.

[34] Roosenboom, E. W. M., Stürmer, A., and Schröder, A., "Advanced Experimental and Numerical Validation and Analysis of Propeller Slipstream Flows," *Journal of Aircraft*, Vol. 47, No. 1, 2010, pp. 284–291. doi:10.2514/1.45961.

[35] Ortun, B., Boisard, R., and Gonzalez-Martino, I., "In-Plane Airloads of a Propeller with Inflow Angle: Prediction vs. Experiment," *30th AIAA Applied Aerodynamics Conference*, AIAA Paper 2012-2778, New Orleans, Louisiana, 2012. doi:10.2514/6.2012-2778.

[36] Spalart, P. R., and Allmaras, S. R., "A One-Equation Turbulence Model for Aerodynamic Flows," *30th Aerospace Sciences Meeting and Exhibit*, AIAA Paper 1992-0439, Reno, Nevada, 1992. doi:10.2514/6.1992-439.

[37] Dacles-Mariani, J., Zilliac, G. G., Chow, J. S., and Bradshaw, P., "Numerical/Experimental Study of a Wingtip Vortex in the near Field," *AIAA Journal*, Vol. 33, No. 9, 1995, pp. 1561–1568. doi:10.2514/3.12826.

[38] Spalart, P. R., and Rumsey, C. L., "Effective Inflow Conditions for Turbulence Models in Aerodynamic Calculations," *AIAA Journal*, Vol. 45, No. 10, 2007, pp. 2544–2553. doi:10.2514/1.29373.

[39] Menter, F. R., "Two-Equation Eddy-Viscosity Turbulence Models for Engineering Applications," *AIAA Journal*, Vol. 32, No. 8, 1994, pp. 1598–1605. doi:10.2514/3.12149.

[40] Stokkermans, T. C. A., van Arnhem, N., Sinnige, T., and Veldhuis, L. L. M., "Validation and Comparison of RANS Propeller Modeling Methods for Tip-Mounted Applications," *AIAA Journal*, Vol. 57, No. 2, 2018, pp. 566–580. doi:10.2514/1.J057398.

[41] Batrakov, A., Kusyumov, A., Mikhailov, S., and Barakos, G., "Aerodynamic Optimization of Helicopter Rear Fuselage," *Aerospace Science and Technology*, Vol. 77, 2018, pp. 704–712. doi:10.1016/j.ast.2018.03.046.

[42] Srinivasan, G. R., Raghavan, V., Duque, E. P. N., and McCroskey, W. J., "Flowfield Analysis of Modern Helicopter Rotors in Hover by Navier-Stokes Method," *Journal of the American Helicopter Society*, Vol. 38, No. 3, 1993, pp. 3–13. doi:10.4050/JAHS.38.3.3.

[43] Johnson, W., *Helicopter Theory*, Courier Corporation, 1994.

[44] Potsdam, M. A., and Strawn, R. C., "CFD Simulations of Tiltrotor Configurations in Hover," *Journal of the American Helicopter Society*, Vol. 50, No. 1, 2005, pp. 82–94. doi:10.4050/1.3092845.

[45] Strawn, R. C., and Djomehri, M. J., "Computational Modeling of Hovering Rotor and Wake Aerodynamics," *Journal of Aircraft*, Vol. 39, No. 5, 2002, pp. 786–793. doi:10.2514/2.3024.

[46] Roache, P. J., "Quantification of Uncertainty in Computational Fluid Dynamics," *Annual Review of Fluid Mechanics*, Vol. 29, No. 1, 1997, pp. 123–160. doi:10.1146/annurev.fluid.29.1.123.

[47] Eça, L., and Hoekstra, M., "Discretization Uncertainty Estimation Based on a Least Squares Version of the Grid Convergence Index," *Proceedings of the Second Workshop on CFD Uncertainty Analysis*, Instituto Superior Tecnico, Lisbon, Portugal, 2006.